MATCH
Communications in Mathematical and in Computer Chemistry

MATCH Commun. Math. Comput. Chem. **97** (2027) 29–77
ISSN: 0340–6253
doi: 10.46793/match.97-1.05626

A Minimal Crowding-Limited Brusselator: Hopf, Turing, and Turing–Hopf Bifurcations Beyond Dilute Kinetics

Qamar Din[a,*]

[a] *Department of Mathematics, University of Poonch Rawalakot, Azad Jammu & Kashmir, Pakistan*

qamar.sms@gmail.com

(Received February 10, 2026)

Abstract

The Brusselator is a canonical model for chemical oscillations and pattern formation under dilute conditions, yet many biochemical and microfluidic settings are crowded and exhibit volume-exclusion effects that reshape effective kinetics. We propose a minimal crowding-limited Brusselator by modifying only the autocatalytic step through a rational free-volume factor that depends on the total local occupancy, while preserving the standard linear feed and decay structure. For the resulting kinetic system, we establish well-posedness together with positivity, boundedness, and permanence, and we derive the unique positive equilibrium. A complete local stability analysis is obtained, including an explicit Hopf threshold and a closed-form evaluation of the first Lyapunov coefficient that determines whether the emerging oscillations are supercritical or subcritical. We then extend the kinetics to a two-dimensional reaction–diffusion system with no-flux boundary conditions and perform a mode-by-mode linearization using the Neumann spectrum. This yields explicit criteria for diffusion-driven (Turing) instability and for a codimension-two Turing–Hopf interaction. A weakly nonlinear reduction provides amplitude equations for the Turing bifurcation and coupled amplitude

*Corresponding author.

equations near the interaction point. Numerical simulations based on a cosine discretization consistent with no-flux boundaries support the analysis and illustrate stationary patterns, temporal oscillations, and mixed breathing spatiotemporal states. Overall, the model offers a tractable bridge between crowding effects and classical oscillatory and pattern-forming dynamics.

1 Introduction

Minimal kinetic models have long served as canonical paradigms for nonlinear chemical oscillations, bifurcations, and self–organization in open (chemostatted) reactors. Among these, the Brusselator occupies a central role as a tractable two–species autocatalytic oscillator, and it is routinely used alongside other archetypal schemes to illustrate how nonlinear feedback can generate sustained oscillations and complex transient behavior in well–mixed settings [9, 11, 20, 25, 27, 30, 33]. Because of its low dimensionality and explicit algebraic structure, the Brusselator also provides a clean testing ground for Hopf bifurcation theory, center–manifold reductions, and normal–form computations that quantify the onset and criticality of oscillations [14, 19, 30].

When spatial transport is incorporated, these same kinetics become a standard laboratory for diffusion–driven instabilities and pattern formation. In particular, reaction–diffusion Brusselator–type systems are classical examples exhibiting stationary Turing patterns and related modal selection mechanisms, with the foundational theory originating in [32] and refined by rigorous instability results and broad pattern–formation frameworks [4,6,10, 15,22]. Experimental demonstrations and empirical pattern phenomenology further motivate their use as benchmark models in nonequilibrium chemistry and morphogenesis [5, 17, 18, 23, 24]. Beyond stationary patterns, the Brusselator family has also been used to probe coupling, synchronization, and collective oscillations in interacting reactors and extended media [1], thereby linking local oscillatory kinetics to macroscopic spatiotemporal organization.

In intracellular and microfluidic environments, however, the dilute mass–action assumption underlying classical kinetic derivations may be-

come questionable. Macromolecular crowding, confinement, and reduced free volume can substantially alter both diffusion and effective reaction propensities by changing encounter rates, screening accessible configuration space, and introducing nontrivial transport corrections [7, 21, 28, 34]. Consequently, rate laws are often replaced by effective kinetics that account for excluded–volume suppression and crowding–induced reductions of reactive flux, especially in regimes where the total local occupancy is no longer small.

Motivated by these observations, we introduce a minimal "crowding–limited" deformation of the Brusselator in which *only* the autocatalytic step is suppressed by a rational free–volume factor depending on the total local occupancy. This choice yields a parsimonious *one–parameter* extension of the classical kinetics: it preserves the linear feed and decay structure of the Brusselator, while encoding crowding through a single scalar parameter that monotonically reduces effective autocatalysis as concentration increases. The resulting model is deliberately designed to remain analytically tractable, so that the principal dynamical consequences of crowding can be derived explicitly rather than inferred only numerically.

The main analytical and computational contributions of this work are as follows. First, we establish a mathematically explicit well–mixed (ODE) model that preserves positivity and admits global a priori bounds, and we prove permanence under a parameter–dependent dissipativity hypothesis. Second, we derive the unique positive equilibrium in closed form, provide explicit feasibility conditions, and obtain an exact Hopf threshold curve with a fully explicit first Lyapunov coefficient, thereby characterizing the Hopf criticality within a complete normal–form framework [14, 19, 30]. Third, we extend the kinetics to a two–dimensional Neumann reaction–diffusion system and carry out a modal linearization consistent with the Neumann cosine spectrum, which is the natural setting for no–flux boundaries. This creates a direct bridge between intracellular crowding concepts [21, 34] and classical diffusion–driven pattern formation theory [6, 8, 15, 22, 32].

Novelty and significance. The novelty lies in the combination of *minimality* and *closed–form bifurcation structure*. By modifying only the

autocatalytic feedback through a single free–volume parameter, we retain the canonical Brusselator architecture while obtaining an analytically transparent framework in which (i) equilibrium feasibility and linear classification, (ii) the Hopf threshold and Hopf criticality, and (iii) diffusion–driven (Turing) and codimension–two Turing–Hopf interactions can be derived explicitly and linked directly to crowding strength. This provides a tractable mechanism to assess how excluded–volume suppression can reorganize the classical oscillation/pattern landscape, while keeping the model sufficiently simple to support reproducible analysis and computation.

The remainder of the paper is organized as follows. Section 2 introduces the crowding–limited Brusselator kinetics, proves well–posedness (positivity, global existence, boundedness), establishes persistence properties, and derives the unique positive equilibrium together with its trace–determinant classification. Section 3 develops the Hopf bifurcation theory of the well–mixed system, including the exact Hopf threshold and an explicit first Lyapunov coefficient that determines supercritical versus subcritical onset. Section 4 formulates the two–dimensional Neumann reaction–diffusion extension, derives the Neumann spectral dispersion relation, and obtains closed–form conditions for Turing instability as well as the codimension–two Turing–Hopf interaction; weakly nonlinear reductions and amplitude equations are also presented. Section 5 provides numerical simulations that verify the analytical predictions for Hopf scaling, diffusion–driven pattern formation, and the emergence of spatiotemporal “breathing” structures near the Turing–Hopf regime. Finally, Section 6 concludes with a summary and brief directions for future work.

2 Model, boundedness, persistence, and local stability

The classical *Brusselator* (introduced as a prototypical autocatalytic oscillator) is based on the reaction network [22, 25]

$$\boxed{\begin{aligned}&\text{(R1) } A \longrightarrow X,\\ &\text{(R2) } B + X \longrightarrow Y + D,\\ &\text{(R3) } 2X + Y \longrightarrow 3X,\\ &\text{(R4) } X \longrightarrow E,\end{aligned}} \tag{1}$$

where A and B are maintained (chemostatted) source species, while D and E represent inert products/outflow.

Crowding/volume-exclusion. To model *crowding* (reduced free volume and diminished effective reaction propensity in dense media), we suppress only the autocatalytic step (R3) by a free–volume factor

$$\phi = \phi(x+y) := \frac{1}{1+\alpha(x+y)}, \qquad \alpha \geq 0,$$

so that increasing total concentration decreases the effective autocatalytic rate. Such free-volume / crowding corrections are standard in biochemical kinetics in dense environments [7, 21, 26, 34] and have also been considered in confined/crowded Brusselator settings and related modifications [2, 31].

Figure 1 summarizes (1) and highlights that only (R3) is crowding-modified.

Crowding-modified ODE model. Following the standard nondimensionalization of the Brusselator [22], the crowding-limited kinetics read

$$\boxed{\begin{aligned}\dot{x} &= A - (B+1)x + \frac{x^2 y}{1+\alpha(x+y)},\\ \dot{y} &= Bx - \frac{x^2 y}{1+\alpha(x+y)},\end{aligned}} \qquad A > 0,\ B > 0,\ \alpha \geq 0, \tag{2}$$

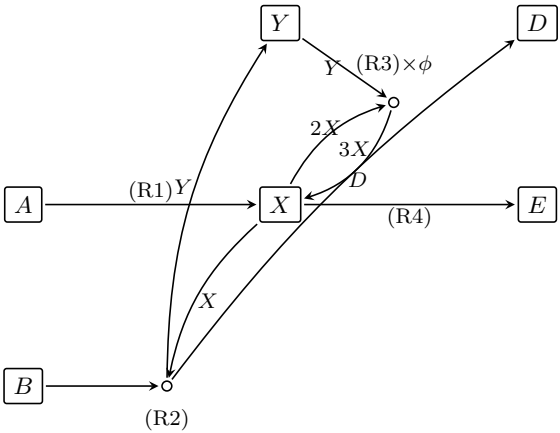

Figure 1. Brusselator reaction scheme with crowding acting only on the autocatalytic step (R3) through the free–volume factor ϕ.

and the total concentration satisfies the affine balance relation

$$\dot{x} + \dot{y} = A - x. \tag{3}$$

Positivity, global existence, and basic a priori bounds

Proposition 1 (Well-posedness and positivity)**.** *For any* $(x(0), y(0)) \in \mathbb{R}^2_{\geq 0}$*, system* (2) *has a unique local solution and*

$$(x(t), y(t)) \in \mathbb{R}^2_{\geq 0} \quad \textit{for all times where the solution exists.}$$

Moreover, if $(x(0), y(0)) \in \mathbb{R}^2_{>0}$*, then* $(x(t), y(t)) \in \mathbb{R}^2_{>0}$ *for all* $t > 0$*.*

Proof. The vector field in (2) is C^1 on $\mathbb{R}^2_{\geq 0}$ since $1 + \alpha(x + y) \geq 1$. On the boundary $x = 0$ one has $\dot{x} = A > 0$, and on the boundary $y = 0$ one has $\dot{y} = Bx \geq 0$. Thus trajectories cannot cross from nonnegative to negative values, proving forward invariance of $\mathbb{R}^2_{\geq 0}$. If $x(0), y(0) > 0$, then $\dot{x}\big|_{x=0} = A > 0$ and $\dot{y}\big|_{y=0} = Bx > 0$ prevent hitting the axes for $t > 0$. ∎

Proposition 2 (Global existence and a linear growth bound)**.** *For any*

$(x(0), y(0)) \in \mathbb{R}^2_{\geq 0}$, *the solution of* (2) *exists for all* $t \geq 0$ *and satisfies*

$$0 \leq x(t) \leq x(t) + y(t) \leq x(0) + y(0) + At, \qquad t \geq 0. \tag{4}$$

Proof. Summing the equations gives (3), hence $\frac{d}{dt}(x+y) = A - x \leq A$ and (4) follows by integration. Since the solution remains finite on every finite interval, the standard continuation theorem for locally Lipschitz ODEs yields global existence. ■

Lemma 1 (Uniform lower bound for the prey component)**.** *For all* $t \geq 0$*,*

$$x(t) \;\geq\; x(0)e^{-(B+1)t} + \frac{A}{B+1}\big(1 - e^{-(B+1)t}\big), \tag{5}$$

and in particular $\liminf_{t\to\infty} x(t) \geq \frac{A}{B+1} > 0$*.*

Proof. Since $\frac{x^2 y}{1+\alpha(x+y)} \geq 0$, from (2) we have $\dot{x} \geq A - (B+1)x$. Comparison with the scalar linear ODE yields (5). ■

Equilibria and a parameter-dependent feasibility condition

Proposition 3 (Equilibria and feasibility)**.** *System* (2) *has no boundary equilibria in* $\mathbb{R}^2_{\geq 0}$*. Moreover, it has a unique positive equilibrium* $E_* = (x_*, y_*) \in \mathbb{R}^2_{>0}$ *given by*

$$\boxed{E_* = (x_*, y_*) := \left(A,\ \frac{B(1+\alpha A)}{A - \alpha B}\right)} \tag{6}$$

provided that

$$\boxed{A > \alpha B.} \tag{7}$$

Proof. If $x = 0$ then $\dot{x} = A > 0$, so no equilibrium can lie on $x = 0$; if $y = 0$ and $x > 0$ then $\dot{y} = Bx > 0$, so no equilibrium lies on $y = 0$. At any equilibrium, (3) gives $x_* = A$. Substituting into $\dot{y} = 0$ yields $BA = \frac{A^2 y_*}{1+\alpha(A+y_*)}$, i.e. $(A - \alpha B)y_* = B(1 + \alpha A)$, hence (6). The positivity condition $y_* > 0$ is equivalent to (7). ■

Ultimate boundedness (dissipativity on bounded sets)

Define the y–nullcline for $x > \alpha B$:

$$y = h(x) := \frac{B(1+\alpha x)}{x - \alpha B}, \qquad x > \alpha B. \tag{8}$$

A direct calculation shows that h is strictly decreasing on $(\alpha B, \infty)$ and $\lim_{x\to\infty} h(x) = \alpha B$.

Theorem 4 (Ultimate boundedness; an explicit parameter condition)**.** *Assume*

$$\boxed{\frac{A}{B+1} > \alpha B \quad \textit{equivalently} \quad A > \alpha B(B+1).} \tag{9}$$

Fix any $\varepsilon \in (0,1)$ *such that* $x_\varepsilon := (1-\varepsilon)\frac{A}{B+1} > \alpha B$ *and set*

$$T_\varepsilon := \frac{1}{B+1}\ln\Big(\frac{1}{\varepsilon}\Big), \qquad \overline{y}_\varepsilon := h(x_\varepsilon) = \frac{B(1+\alpha x_\varepsilon)}{x_\varepsilon - \alpha B}. \tag{10}$$

Then every solution of (2) *with* $(x(0), y(0)) \in \mathbb{R}^2_{\geq 0}$ *satisfies*

$$y(t) \leq \max\{y(T_\varepsilon), \overline{y}_\varepsilon\} \qquad \textit{for all } t \geq T_\varepsilon, \tag{11}$$

and consequently

$$x(t) + y(t) \leq \max\big\{x(T_\varepsilon) + y(T_\varepsilon),\ A + \max\{y(T_\varepsilon), \overline{y}_\varepsilon\}\big\} \qquad \textit{for all } t \geq T_\varepsilon. \tag{12}$$

In particular, the semiflow generated by (2) *is point-dissipative on bounded sets: for every* $R > 0$ *there exists* $M(R) > 0$ *such that all solutions with* $x(0) + y(0) \leq R$ *satisfy* $x(t) + y(t) \leq M(R)$ *for all sufficiently large* t*.*

Proof. From Lemma 1 we have $x(t) \geq (1 - e^{-(B+1)t})\frac{A}{B+1}$, hence $x(t) \geq x_\varepsilon$ for all $t \geq T_\varepsilon$. For $x > \alpha B$, the condition $\dot{y} = 0$ is equivalent to $y = h(x)$ in (8); moreover, $\dot{y} > 0$ for $0 < y < h(x)$ and $\dot{y} < 0$ for $y > h(x)$ (e.g. by inspecting the sign of $\dot{y}$ for large y and using uniqueness of the nullcline). Since h is decreasing and $x(t) \geq x_\varepsilon$ for $t \geq T_\varepsilon$, we have $h(x(t)) \leq h(x_\varepsilon) = \overline{y}_\varepsilon$, hence $\dot{y}(t) < 0$ whenever $t \geq T_\varepsilon$ and $y(t) > \overline{y}_\varepsilon$. This yields (11).

Let $z = x + y$. For $t \geq T_\varepsilon$ we have $y(t) \leq Y_\varepsilon := \max\{y(T_\varepsilon), \overline{y}_\varepsilon\}$ and

therefore $x(t) = z(t) - y(t) \geq z(t) - Y_\varepsilon$, so

$$\dot{z} = A - x \leq A - (z - Y_\varepsilon) = (A + Y_\varepsilon) - z.$$

A comparison argument with the linear ODE $\dot{w} = (A + Y_\varepsilon) - w$ gives (12). The final statement follows because $z(T_\varepsilon) \leq R + AT_\varepsilon$ for all initial data with $z(0) \leq R$ by Proposition 2. ■

Uniform persistence (permanence)

Theorem 5 (Permanence under (9))**.** *Assume* (9)*. Then every solution with* $(x(0), y(0)) \in \mathbb{R}^2_{>0}$ *is permanent on bounded sets in the sense of persistence theory [3, 16, 29]: for each* $R > 0$ *there exist constants* $0 < m(R) < M(R)$ *such that if* $x(0)+y(0) \leq R$*, then the corresponding solution satisfies, for all sufficiently large* t*,*

$$m(R) \leq x(t) \leq M(R), \qquad m(R) \leq y(t) \leq M(R).$$

In particular, both components remain bounded away from 0 *and from* ∞ *uniformly for all interior solutions issued from the bounded set* $\{x + y \leq R\} \cap \mathbb{R}^2_{>0}$*.*

Proof. Fix $R > 0$. By Lemma 1, choosing $\varepsilon = \frac{1}{2}$ yields a time $T_0 = \frac{\ln 2}{B+1}$ such that $x(t) \geq \frac{A}{2(B+1)} =: x_{\min}$ for all $t \geq T_0$. By Theorem 4 there is $M(R) > 0$ and $T_1 \geq T_0$ such that $0 < x(t), y(t) \leq M(R)$ for all $t \geq T_1$.

Using $1 + \alpha(x + y) \geq 1$, from (2) we obtain

$$\dot{y} = Bx - \frac{x^2 y}{1 + \alpha(x + y)} \;\geq\; Bx - x^2 y \;\geq\; Bx_{\min} - M(R)^2\, y, \qquad t \geq T_1.$$

Comparison with the scalar linear ODE $\dot{v} = Bx_{\min} - M(R)^2 v$ gives

$$\liminf_{t\to\infty} y(t) \;\geq\; \frac{B\, x_{\min}}{M(R)^2} \;=:\; y_{\min}(R) > 0.$$

Finally, permanence for x follows from the explicit lower bound in Lemma 1 (so $\liminf x(t) \geq A/(B + 1)$), together with the uniform upper bounds already obtained. Setting $m(R) := \min\{A/(2(B + 1)),\, y_{\min}(R)\}$ completes

the proof. ■

Remark. Condition (7) guarantees existence of the unique positive equilibrium E_*. The stronger condition (9) is a convenient sufficient hypothesis ensuring that for large times the prey component stays uniformly above αB, which makes the decreasing y–nullcline (8) available for an explicit trapping argument.

Local stability analysis

Assume that $A > \alpha B$, then the Jacobian $J(E_*)$ at positive equilibrium E_* is given by:

$$J(E_*) = \begin{pmatrix} \frac{B-\alpha A+\alpha^2 B^2-1}{\alpha A+1} & \frac{(A-\alpha B)^2}{\alpha A+1} \\ -\frac{B\left(\alpha^2 B+1\right)}{\alpha A+1} & -\frac{(A-\alpha B)^2}{\alpha A+1} \end{pmatrix}. \tag{13}$$

Let τ and δ denote trace and determinant of $J(E_*)$, respectively, then we have

$$\tau := \frac{B - A(\alpha + A - 2\alpha B) - 1}{\alpha A + 1},\ \delta := \frac{(A - \alpha B)^2}{\alpha A + 1} > 0. \tag{14}$$

Consequently, the characteristic polynomial of $J(E_*)$ is given by

$$F(\lambda) = \lambda^2 - \left(\frac{B - A(\alpha + A - 2\alpha B) - 1}{\alpha A + 1}\right)\lambda + \frac{(A - \alpha B)^2}{\alpha A + 1}. \tag{15}$$

Let Δ be the discriminant of (15), then one can easily obtain:

$$\Delta := \tau^2 - 4\delta = \frac{(A(\alpha + A - 2\alpha B) - B + 1)^2 - 4(\alpha A + 1)(A - \alpha B)^2}{(\alpha A + 1)^2}.$$

Theorem 6 (Topological classification of E_*)**.** *Assume $A > \alpha B$ so that E_* exists. Then $\delta > 0$ and E_* cannot be a saddle. Moreover, the local behavior of E_* is completely determined by τ and Δ in (trace–determinant classification [19, 30]):*

(i) If $\tau < 0$ and $\Delta > 0$, then E_* is a stable node.

(ii) If $\tau < 0$ and $\Delta < 0$, then E_* is a stable focus (spiral sink).

(iii) If $\tau > 0$ and $\Delta > 0$, then E_* is an unstable node.

(iv) If $\tau > 0$ and $\Delta < 0$, then E_* is an unstable focus (spiral source).

(v) If $\Delta = 0$ and $\tau \neq 0$, then E_* is a degenerate (improper) node.

(vi) If $\tau = 0$ (equivalently)

$$\boxed{A^2 = B - 1 + \alpha A(2B - 1),} \tag{16}$$

then the linearization has purely imaginary eigenvalues provided $\delta > 0$ (automatic under $A > \alpha B$), which is the standard Hopf threshold in the trace–determinant plane; generically this corresponds to a Hopf bifurcation once the usual nondegeneracy conditions are verified [14, 19].

Remark. Since $1 + \alpha A > 0$, the sign of τ is determined by its numerator $B - A(\alpha + A - 2\alpha B) - 1$. Thus E_* is linearly stable (sink) if and only if

$$A^2 > B - 1 + \alpha A(2B - 1),$$

and unstable (source) if the inequality is reversed. The node/focus distinction is then decided by the sign of Δ.

Moreover, at $A = 2.2$, the topological classification related to Theorem 6 is depicted in Fig. 2.

3 Hopf bifurcation

We analyze the Hopf bifurcation of the unique positive equilibrium $E_* = (x_*, y_*)$ of the crowding-modified Brusselator (2) by taking B as the bifurcation parameter, with $A > 0$ and $\alpha \geq 0$ fixed. Recall that $x_* \equiv A$ and

$$y_*(B) = \frac{B(1 + \alpha A)}{A - \alpha B}, \qquad \text{so } E_*(B) \in \mathbb{R}^2_{>0} \iff A > \alpha B.$$

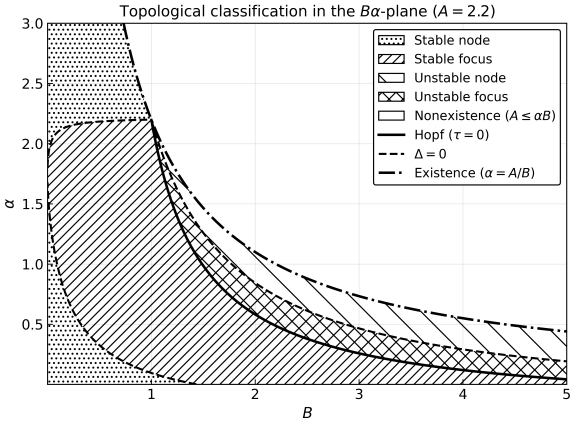

Figure 2. Topological classification in the B–α plane for the crowding-modified Brusselator (2) with $A = 2.2$. Shaded (hatched) regions indicate stable/unstable node/focus types of the coexistence equilibrium E_* whenever it exists ($A > \alpha B$). The Hopf curve ($\tau = 0$) is shown as a solid line, the discriminant curve ($\Delta = 0$) as a dashed line, and the existence boundary $\alpha = A/B$ as a dash–dot line.

Taking τ, that is, the trace of $J(E_*)$ as follows:

$$\tau(B) = \operatorname{tr}(J(E_*(B))) = \frac{-A^2 + 2\alpha AB - \alpha A + B - 1}{1 + \alpha A}. \tag{17}$$

Hence the Hopf threshold $\tau(B) = 0$ occurs at

$$\boxed{B = B_H(A, \alpha) := \frac{A^2 + \alpha A + 1}{1 + 2\alpha A}.} \tag{18}$$

At $B = B_H$ the feasibility condition becomes $A > \alpha B_H \iff A > \alpha$ (since $A - \alpha B_H = \frac{(A-\alpha)(1+\alpha A)}{1+2\alpha A}$). Thus, throughout this section we assume

$$\boxed{A > \alpha \geq 0,} \tag{19}$$

so that the equilibrium E_* exists at $B = B_H$.

Introduce the unfolding parameter

$$\boxed{\mu := B - B_H,} \tag{20}$$

so that $\mu = 0$ corresponds to the Hopf point. Since (17) is affine in B,

$$\tau(B) = \tau_B\,\mu, \tau_B := \frac{d\tau}{dB} = \frac{1+2\alpha A}{1+\alpha A} > 0. \tag{21}$$

In particular, the equilibrium is a sink for $\mu < 0$ and a source for $\mu > 0$ (stability changes from stable to unstable as B increases through B_H).

At $E_*(B)$ one has $\delta(B) := \det(J(E_*(B))) = \frac{(A-\alpha B)^2}{1+\alpha A} > 0$. At the Hopf point $\mu = 0$ (i.e. $B = B_H$), the linearization has eigenvalues $\lambda_{1,2} = \pm i\omega_H$, where

$$\omega_H = \sqrt{\delta(B_H)} = \frac{(A-\alpha)\sqrt{1+\alpha A}}{1+2\alpha A} > 0. \tag{22}$$

Moreover, the Hopf equilibrium is

$$E_H = (x_H, y_H) := (A, y_H), y_H := y_*(B_H) = \frac{A^2+\alpha A+1}{A-\alpha}. \tag{23}$$

Let (u, v) be translated coordinates about E_H:

$$x = A + u, \qquad y = y_H + v. \tag{24}$$

At $\mu = 0$ the Jacobian takes the closed form

$$J_H := J(E_H) = \begin{pmatrix} \omega_H^2 & \omega_H^2 \\ -(1+\omega_H^2) & -\omega_H^2 \end{pmatrix},\ \mathrm{tr}(J_H) = 0,\ \det(J_H) = \omega_H^2. \tag{25}$$

Define the real similarity matrix built from $\Re(q)$ and $\Im(q)$, where q is an eigenvector of J_H for $i\omega_H$:

$$q = \begin{pmatrix} 1 \\ -1 + i/\omega_H \end{pmatrix}, P := \begin{bmatrix} \Re(q)\ \Im(q) \end{bmatrix} = \begin{pmatrix} 1 & 0 \\ -1 & 1/\omega_H \end{pmatrix},\ \det P = \frac{1}{\omega_H} \neq 0.$$

Then a direct computation yields the canonical (rotation) form

$$P^{-1}J_H P = \begin{pmatrix} 0 & -\omega_H \\ \omega_H & 0 \end{pmatrix}. \tag{26}$$

Thus, introducing (X, Y) by

$$\begin{pmatrix} u \\ v \end{pmatrix} = P \begin{pmatrix} X \\ Y \end{pmatrix}, \tag{27}$$

the linear part at $\mu = 0$ becomes the standard planar oscillator.

Write the shifted system (at $\mu = 0$) in the standard polynomial form

$$\begin{aligned} \dot{u} &= a_{10}u + a_{01}v + \frac{1}{2}\big(a_{20}u^2 + 2a_{11}uv + a_{02}v^2\big) \\ &\quad + \frac{1}{6}\big(a_{30}u^3 + 3a_{21}u^2v + 3a_{12}uv^2 + a_{03}v^3\big) + \mathcal{O}(\|(u,v)\|^4), \\ \dot{v} &= b_{10}u + b_{01}v + \frac{1}{2}\big(b_{20}u^2 + 2b_{11}uv + b_{02}v^2\big) \\ &\quad + \frac{1}{6}\big(b_{30}u^3 + 3b_{21}u^2v + 3b_{12}uv^2 + b_{03}v^3\big) + \mathcal{O}(\|(u,v)\|^4), \end{aligned} \tag{28}$$

where a_{ij} and b_{ij} are the corresponding partial derivatives of the vector field evaluated at $(x, y) = (A, y_H)$ and $B = B_H$.

At the Hopf point ($\mu = 0$), these coefficients simplify to the following closed forms (depending only on A and α):

$$a_{10} = a_{01} = \omega_H^2, b_{01} = -\omega_H^2, b_{10} = -\frac{(A^2 + \alpha A + 1)(\alpha A + \alpha^2 + 1)}{(1 + 2\alpha A)^2}. \tag{29}$$

The quadratic coefficients are

$$\begin{aligned} a_{20} &= \frac{2(A^2 + \alpha A + 1)(\alpha A + \alpha^2 + 1)^2}{A(1 + 2\alpha A)^3}, \\ a_{11} &= \frac{(A - \alpha)^2\big(4A^2\alpha^2 + 2A\alpha^3 + 5A\alpha + 2\alpha^2 + 2\big)}{A(1 + 2\alpha A)^3}, \\ a_{02} &= -\frac{2\alpha(A - \alpha)^3(1 + \alpha A)}{A(1 + 2\alpha A)^3}, \end{aligned} \qquad \begin{aligned} b_{20} &= -a_{20}, \\ b_{11} &= -a_{11}, \\ b_{02} &= -a_{02}. \end{aligned} \tag{30}$$

The cubic coefficients are

$$\begin{aligned}
a_{30} &= -\frac{6\alpha(A-\alpha)(A^2+\alpha A+1)(\alpha A+\alpha^2+1)^2}{A^2(1+2\alpha A)^4},\\
a_{21} &= \frac{2(A-\alpha)^2(\alpha A+\alpha^2+1)\big(3A^2\alpha^2+3A\alpha^3+2A\alpha+3\alpha^2+1\big)}{A^2(1+2\alpha A)^4},\\
a_{12} &= -\frac{2\alpha(A-\alpha)^3\big(3A^2\alpha^2+3A\alpha^3+4A\alpha+3\alpha^2+2\big)}{A^2(1+2\alpha A)^4},\\
a_{03} &= \frac{6\alpha^2(A-\alpha)^4(1+\alpha A)}{A^2(1+2\alpha A)^4},
\end{aligned} \tag{31}$$

and

$$b_{30}=-a_{30}, b_{21}=-a_{21}, b_{12}=-a_{12}, b_{03}=-a_{03}.$$

Let $\lambda(\mu)$ denote the eigenvalue of the linearization at $E_*(B)$ with $\Im\lambda(\mu)>0$. Since $\Re\lambda(\mu)=\frac{1}{2}\tau(B)$ for a planar system, (21) yields

$$\boxed{\left.\frac{d}{d\mu}\Re\lambda(\mu)\right|_{\mu=0}=\frac{1}{2}\,\tau_B=\frac{1+2\alpha A}{2(1+\alpha A)}\neq 0,} \tag{32}$$

so the Hopf crossing is transversal.

In the canonical coordinates (27), set $z=X+iY$. Standard Hopf normal-form theory (e.g. the Kuznetsov/Hassard multilinear-form formula) [14, 19] gives, after a near-identity transformation,

$$\boxed{\dot z=\big(\kappa\mu+i\omega_H\big)z+\ell_1\,z|z|^2+\mathcal{O}\big(|z|^4+|\mu||z|^2+\mu^2|z|\big),} \tag{33}$$

where the unfolding slope is

$$\boxed{\kappa=\frac{1}{2}\tau_B=\frac{1+2\alpha A}{2(1+\alpha A)}>0,} \tag{34}$$

and the *first Lyapunov coefficient* ℓ_1 is obtained explicitly as

$$\ell_1=\frac{1}{2\omega_H}\Re(c_1),$$

with c_1 given by the standard bilinear/trilinear expression in terms of the

second and third derivatives of the vector field at the Hopf point (see [14,19], and Appendix A).

For (2), evaluating at $(x, y, B) = (A, y_H, B_H)$ and simplifying yields the closed form (see Appendix A):

$$\boxed{\ell_1(A,\alpha) = -\frac{6A^2\alpha^2 + 6A\alpha + A^2 + 2}{4A^2(1+\alpha A)^{3/2}(A-\alpha)}} \tag{35}$$

Equivalently, one may write

$$\ell_1(A,\alpha) = -\frac{A^2 + 2 + 6A\alpha(1+A\alpha)}{4A^2(1+\alpha A)^{3/2}(A-\alpha)}.$$

Remark. (i) In the classical Brusselator limit $\alpha = 0$, (35) reduces to

$$\ell_1(A,0) = -\frac{A^2+2}{4A^3},$$

which is the standard Hopf coefficient at $B = A^2+1$. (ii) For the biologically feasible Hopf point (in particular $A > \alpha$ and $\alpha \geq 0$), the denominator in (35) is positive and the numerator is strictly positive; hence

$$\ell_1(A,\alpha) < 0.$$

Therefore, the Hopf bifurcation at E_* is *supercritical* (a stable small-amplitude limit cycle is born as the Hopf parameter crosses the threshold, under the usual nondegeneracy/transversality assumptions).

The nondegeneracy condition for a *generic* Hopf bifurcation is

$$\boxed{\ell_1(A,\alpha) \neq 0.} \tag{36}$$

In addition, *transversality* requires $\kappa \neq 0$ in the normal form (33). Since $\kappa > 0$ (as shown above), the equilibrium branch $E_*(B)$ changes from *stable* to *unstable* as B increases through B_H, i.e., as $\mu := B - B_H$ crosses 0 from negative to positive. The sign of ℓ_1 determines the Hopf criticality.

Theorem 7 (Hopf bifurcation at $B = B_H$)**.** *Assume $A > \alpha \geq 0$ and let B_H and ω_H be given by* (18)–(22)*. Then system* (2) *undergoes a transversal*

Hopf bifurcation of the equilibrium branch $E_*(B)$ at $B = B_H$. Moreover, the first Lyapunov coefficient is given by (35) and satisfies $\ell_1(A, \alpha) < 0$; hence the Hopf bifurcation is supercritical. In particular, for $\mu > 0$ (i.e. $B > B_H$) there exists a stable small-amplitude periodic orbit emanating from $E_*(B)$, while $E_*(B)$ becomes unstable for $\mu > 0$.

Computational verification (supercritical case). Fix, for instance, $A = 1.5$ and $\alpha = 0.3$. Then (18) gives

$$B_H = \frac{A^2 + \alpha A + 1}{1 + 2\alpha A} = 1.947368421,$$
$$\omega_H = \frac{(A - \alpha)\sqrt{1 + \alpha A}}{1 + 2\alpha A} = 0.760521763.$$

and the closed-form formula (35) yields

$$\ell_1(1.5, 0.3) \approx -0.43299256 < 0,$$

so the theory predicts a *supercritical* Hopf bifurcation: as $\mu := B - B_H > 0$, a small attracting limit cycle is born from $E_*(B)$.

To confirm this numerically, we integrate (2) for a sequence of small $\mu > 0$ (e.g. $\mu \in \{10^{-3}, 2 \cdot 10^{-3}, 5 \cdot 10^{-3}\}$) using an adaptive time integrator (such as RK45) with initial data $x(0) = A + 10^{-3}$ and $y(0) = y_*(B_H + \mu) + 10^{-3}$, and discard a sufficiently long transient. Using the linear canonical coordinates at Hopf (cf. (26)),

$$u = x - A, \quad v = y - y_H, \; X = u, \; Y = \omega_H(u + v), \; \rho(t) = \sqrt{X(t)^2 + Y(t)^2},$$

we define the post-transient mean-square amplitude by

$$r(\mu) := \langle \rho(t)^2 \rangle,$$

where $\langle \cdot \rangle$ denotes time averaging over the post-transient window. Numerically, the resulting amplitude satisfies the expected Hopf scaling: a log–log fit yields $\rho(\mu) \propto \mu^{1/2}$ (equivalently $r(\mu) \propto \mu$), and stable periodic orbits are observed only for $B > B_H$, consistent with $\ell_1(1.5, 0.3) < 0$ and Theorem 7.

Figure 3 provides a numerical verification of the Hopf bifurcation at the homogeneous coexistence equilibrium. For $B < B_H$ the equilibrium is stable, while for $B > B_H$ a family of stable periodic orbits is observed, as evidenced by the separation of post-transient extrema in panels (a)–(b) and the phase portraits in panel (c). Moreover, the log–log scaling in panel (d) shows $A_x(\mu)^2, A_y(\mu)^2 \propto \mu$ with $\mu = B - B_H > 0$, which is the standard supercritical Hopf scaling predicted by the Stuart–Landau normal form; cf. [13, 19].

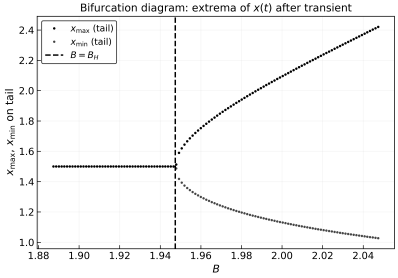

(a) Bifurcation diagram (ODE): extrema of $x(t)$ after transient.

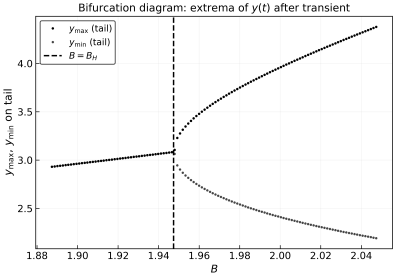

(b) Bifurcation diagram (ODE): extrema of $y(t)$ after transient.

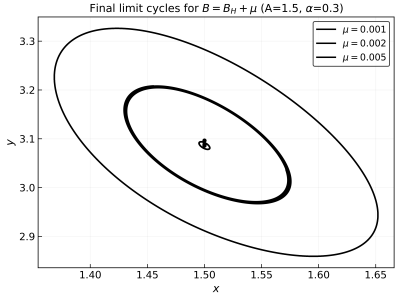

(c) Phase portraits: stable limit cycles for $B = B_H + \mu$ (several $\mu > 0$).

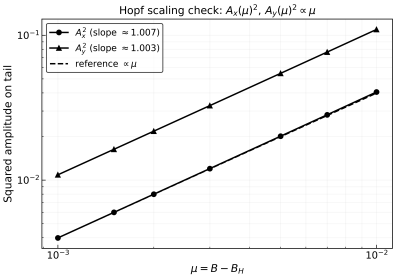

(d) Hopf scaling check: $A_x(\mu)^2$ and $A_y(\mu)^2$ vs $\mu = B - B_H$ (log–log).

Figure 3. Numerical verification of the Hopf bifurcation at the homogeneous coexistence equilibrium. Panels (a)–(b) show the emergence of oscillations through extrema of each component after discarding transients; panel (c) shows representative limit cycles; panel (d) confirms the normal-form scaling $A(\mu)^2 \propto \mu$, consistent with a supercritical Hopf bifurcation.

4 A Neumann 2D reaction–diffusion extension

To incorporate spatial effects, we consider the crowding–limited Brusselator kinetics in two space dimensions on the rectangle $\Omega = (0, L_x) \times (0, L_y)$:

$$\boxed{\begin{aligned} u_t &= D_u \Delta u + f(u, v), \\ v_t &= D_v \Delta v + g(u, v), \end{aligned}} \qquad (x, y) \in \Omega,\ t > 0, \tag{37}$$

with **Neumann boundary conditions**

$$\partial_n u = \partial_n v = 0 \quad \text{on } \partial\Omega,$$

where $D_u, D_v > 0$ and

$$f(u, v) = A - (B+1)u + \frac{u^2 v}{1 + \alpha(u+v)}, g(u, v) = Bu - \frac{u^2 v}{1 + \alpha(u+v)}, \tag{38}$$

with $A, B, \alpha > 0$. We use (u, v) for the spatially distributed concentrations; the *homogeneous* equilibria coincide with those of the well–mixed ODE system studied earlier.

4.1 Well–posedness and positivity under Neumann BC

Let $(u_0, v_0) \in C(\overline{\Omega})^2$ satisfy $u_0 \geq 0$, $v_0 \geq 0$. The reaction field (38) is C^∞ on $\mathbb{R}^2_{\geq 0}$ and is *quasi–positive*: $f(0, v) = A \geq 0$ and $g(u, 0) = Bu \geq 0$ for $u, v \geq 0$. Standard semilinear parabolic theory then yields the following invariance property (see, e.g., classical reaction–diffusion references cited in [12, 22]).

Lemma 2 (Positivity and forward invariance)**.** *For any nonnegative initial data $(u_0, v_0) \in C(\overline{\Omega})^2$, the system (37)–(38) admits a unique local classical solution $(u, v) \in C^{2,1}(\overline{\Omega} \times (0, T_{\max}))^2$, and*

$$u(x, y, t) \geq 0, \qquad v(x, y, t) \geq 0 \qquad \textit{for all } (x, y) \in \overline{\Omega},\ t \in (0, T_{\max}).$$

Remark (On global existence/bounds). For the pattern–formation analysis below, it suffices that solutions exist long enough to observe the linear instability and the ensuing weakly nonlinear saturation. Global existence and boundedness for Brusselator–type systems with Neumann BC are classical; see [12, 22] and references therein.

4.2 Neumann spectrum and modal linearization

Under Neumann BC, the Laplacian eigenfunctions are cosine modes

$$\phi_{mn}(x,y) = \cos\Big(\frac{m\pi x}{L_x}\Big)\cos\Big(\frac{n\pi y}{L_y}\Big),\ k_{mn}^2 = \Big(\frac{m\pi}{L_x}\Big)^2 + \Big(\frac{n\pi}{L_y}\Big)^2,\ m,n \in \mathbb{N}_0.$$

Let $E_* = (u^*, v^*)$ be the positive homogeneous equilibrium (the same $E_* = (x^*, y^*)$ from the ODE analysis). In particular, under the feasibility condition from the ODE part,

$$u^* = A, \qquad v^* = \frac{B(1+\alpha A)}{A - \alpha B},\ \text{requiring } A > \alpha B. \tag{39}$$

Let

$$J_* = \begin{pmatrix} f_u^* & f_v^* \\ g_u^* & g_v^* \end{pmatrix}$$

denote the Jacobian of (f, g) at E_*, whose *closed form* entries $f_u^*, f_v^*, g_u^*, g_v^*$ were already derived in $J(E_*)$ (cf. (13)). We also recall from the ODE part the scalar invariants, using the same notation as in Section 3:

$$\tau := \mathrm{tr}(J_*), \qquad \delta := \det(J_*), \qquad \Delta := \tau^2 - 4\delta. \tag{40}$$

(Thus, throughout the RD analysis, δ denotes the determinant and Δ denotes the discriminant.)

Linearizing (37) at the spatially homogeneous state E_* and projecting onto a Neumann mode ϕ_{mn} leads to the 2×2 eigenvalue problem

$$\partial_t \mathbf{w} = \big(J_* - k_{mn}^2 D\big)\mathbf{w}, \qquad D = \mathrm{diag}(D_u, D_v),$$

and thus to the *dispersion relation*

$$\lambda^2 - \tau(k)\lambda + \delta(k) = 0, \tag{41}$$

where, writing $k^2 = k_{mn}^2$ for brevity,

$$\tau(k) = \tau - (D_u + D_v)k^2, \delta(k) = \delta - \big(D_u g_v^* + D_v f_u^*\big)k^2 + D_u D_v k^4. \tag{42}$$

Hence a mode $k > 0$ is unstable iff (41) has a root with $\Re\lambda > 0$.

4.3 Hopf instability of the homogeneous mode ($k = 0$)

The homogeneous mode corresponds to $k = 0$, for which (41) reduces to the ODE characteristic polynomial. Therefore, **the Hopf curve is unchanged by diffusion**: the Hopf bifurcation of the spatially homogeneous equilibrium occurs at the same parameter locus as in the well–mixed system (see (18)), and its criticality is governed by the same first Lyapunov coefficient $\ell_1(A, \alpha)$ computed earlier (see Theorem 7).

Remark (No oscillatory finite–k instability near the ODE Hopf point). If the ODE is at Hopf, $\tau = 0$ and $\delta > 0$. Then for every $k > 0$, $\tau(k) = -(D_u + D_v)k^2 < 0$, so no Neumann mode with $k > 0$ can satisfy $\tau(k) = 0$ in a neighborhood of the ODE Hopf point. Thus diffusion does not create a nearby oscillatory instability at $k > 0$; the competing diffusion–driven instability is of *stationary* (Turing) type.

4.4 Diffusion–driven (Turing) instability

Assume the ODE equilibrium is linearly asymptotically stable:

$$\tau < 0, \qquad \delta > 0. \tag{43}$$

Then $\tau(k) < 0$ for all $k \geq 0$ by (42). Hence a diffusion–driven instability can only occur if $\delta(k) < 0$ for some admissible Neumann mode $k > 0$.

Define the *cross–diffusive trace combination*

$$Q := D_u g_v^* + D_v f_u^*. \tag{44}$$

Since $\delta(k)$ is a quadratic polynomial in k^2 with leading coefficient $D_u D_v > 0$, its minimum over $k^2 \geq 0$ occurs at $k^2 = Q/(2D_u D_v)$ provided $Q > 0$.

Theorem 8 (Turing instability conditions)**.** *Assume* (43)*. Then there exists a Neumann mode $k > 0$ such that E_* is unstable for the reaction–diffusion system* (37) *iff*

$$Q > 0, \qquad Q^2 > 4D_u D_v\, \delta. \tag{45}$$

In that case, the unstable band in k^2 is

$$k_-^2 < k^2 < k_+^2, \qquad k_\pm^2 = \frac{Q \pm \sqrt{Q^2 - 4D_u D_v\, \delta}}{2D_u D_v},$$

and the fastest growing wavenumber (in the continuous–k idealization) is

$$k_*^2 = \frac{Q}{2D_u D_v}. \tag{46}$$

On the bounded domain, one observes patterns when an admissible Neumann eigenvalue k_{mn}^2 lies in (k_-^2, k_+^2), typically the one closest to k_*^2.

The *Turing threshold* (marginal diffusion–driven instability) occurs when

$$Q > 0, \qquad Q^2 = 4D_u D_v\, \delta, \tag{47}$$

in which case the critical wavenumber is

$$k_c^2 = \frac{Q}{2D_u D_v}. \tag{48}$$

For our crowding–limited kinetics, Q and δ admit closed forms in parameters, see Appendix B.

Remark (Classical interpretation)*.* Conditions (45) are the standard diffusion–driven pattern criteria (stable ODE, unstable PDE) in the sense of [4, 6, 22].

4.5 Turing–Hopf (Hopf–Turing) codimension–two interaction

In addition to pure Turing instability (stable kinetics, unstable spatial modes), the Neumann reaction–diffusion system (37) can exhibit a *Turing–Hopf* (also called Hopf–Turing) codimension–two interaction in which the homogeneous mode $k = 0$ is at a Hopf threshold while a finite Neumann mode $k = k_c > 0$ is simultaneously at the onset of diffusion–driven instability. Such mode interactions are a standard organizing mechanism in pattern formation theory (see, e.g., [6, 15, 22]).

Definition (Turing–Hopf point). Fix $A > 0$, $\alpha \geq 0$ and $D_u > 0$. We treat (B, D_v) as unfolding parameters. Let (u^*, v^*) be the homogeneous equilibrium from Section 2 and denote the kinetic Jacobian at (u^*, v^*) by J with invariants

$$\tau = \operatorname{tr}(J), \qquad \delta = \det(J),$$

as in (14). For a Neumann wavenumber $k \geq 0$, the linearized dispersion relation is

$$\lambda^2 - \tau(k)\lambda + \delta(k) = 0, \tau(k) = \tau - (D_u + D_v)k^2, \delta(k) = \delta - Q\,k^2 + D_u D_v k^4,$$

where $Q := D_u g_v + D_v f_u$ (cf. Section 4). A *Turing–Hopf point* is a parameter pair (B, D_v) for which

$$\tau = 0,\ \delta > 0,\ Q > 0, \quad Q^2 = 4D_u D_v \delta,\ k_c^2 = \frac{Q}{2D_u D_v} > 0, \tag{49}$$

so that $\lambda = \pm i\sqrt{\delta}$ at $k = 0$ and $\lambda = 0$ at $k = k_c$ (continuous-spectrum threshold).

Proposition 9 (Closed-form Turing–Hopf point in (B, D_v))**.** *Assume $A > \alpha$ so that the Hopf curve $B = B_H(A, \alpha)$ from (18) lies inside the existence region $A > \alpha B$. Let $B = B_H$ and denote*

$$\delta_H := \delta\big|_{B=B_H} = \frac{(A-\alpha)^2(1+\alpha A)}{(1+2\alpha A)^2} > 0. \tag{50}$$

Then the diffusion contrast values D_v for which the Hopf threshold at $k = 0$

coincides with the Turing threshold at a finite mode are given by

$$\boxed{D_v^{TH,\pm} = D_u \frac{\delta_H + 2 \pm 2\sqrt{\delta_H + 1}}{\delta_H} = D_u \frac{\left(\sqrt{\delta_H + 1} \pm 1\right)^2}{\delta_H}.} \tag{51}$$

The physically relevant diffusion-contrast branch is typically $D_v^{TH,+} > D_u$. *The associated critical wavenumber at the codimension–two point is*

$$\boxed{k_c^2 = \frac{\delta_H \left(D_v^{TH,+} - D_u\right)}{2 D_u D_v^{TH,+}}.} \tag{52}$$

Proof. At $B = B_H$ we have $\tau = 0$ and $\delta = \delta_H > 0$ (Section 3). A key simplification at Hopf is $f_u = \delta_H$ and $g_v = -\delta_H$ (proved in Appendix C), hence $Q = D_u g_v + D_v f_u = \delta_H (D_v - D_u)$. The continuous Turing-threshold condition $Q^2 = 4 D_u D_v \delta_H$ becomes $\delta_H (D_v - D_u)^2 = 4 D_u D_v$, which yields the quadratic formula (51). Finally $k_c^2 = Q/(2 D_u D_v)$ gives (52). ∎

Remark (Discrete Neumann spectrum). On a bounded Neumann domain, admissible wavenumbers are discrete: $k = k_{mn}$. Thus, in simulations one observes the Turing–Hopf interaction most cleanly when the critical value (52) is close to some admissible k_{mn}^2 (and the corresponding eigenvalue is simple). In practice, one chooses (B, D_v) near the continuous codimension–two point so that a single Neumann mode dominates the spatial structure, while Hopf dynamics drives temporal oscillations.

Remark (Amplitude equations near Turing–Hopf). Near (49), the center manifold is (generically) three-dimensional: one complex Hopf mode ($k = 0$) and one real Turing mode ($k = k_c$). A standard multiple-scales reduction yields coupled amplitude equations of the form

$$\boxed{\begin{aligned} \dot{A} &= (\mu_H + i\omega_H) A + a_1 A |A|^2 + a_2 A Z^2 + \mathcal{O}(4), \\ \dot{Z} &= \mu_T Z + b_1 Z^3 + b_2 Z |A|^2 + \mathcal{O}(4), \end{aligned}} \tag{53}$$

where $A \in \mathbb{C}$ is the Hopf amplitude, $Z \in \mathbb{R}$ is the Turing amplitude, and μ_H, μ_T are unfolding parameters proportional to $(B - B_H)$ and $(D_v - D_v^{TH,+})$. All coefficients a_j, b_j can be written explicitly in closed form in

terms of the multilinear forms of the reaction vector field evaluated at (u^*, v^*); see Appendix C.

4.6 Turing bifurcation and amplitude equation

Near the stationary instability (47)–(48), one can perform a center–manifold (multiple–scales) reduction (see [6, 15]) to obtain a real Landau amplitude equation for the critical Neumann mode. Let μ_T be a scalar unfolding parameter measuring signed distance to the Turing curve (e.g. $\mu_T = B - B_T$ when B is varied across the Turing threshold with other parameters fixed). Then the leading-order slow dynamics of the critical amplitude $\mathcal{A}(T)$ takes the form

$$\boxed{\frac{d\mathcal{A}}{dT} = \sigma_T\,\mu_T\,\mathcal{A} - g_T\,\mathcal{A}^3 + \mathcal{O}(|\mathcal{A}|^5, |\mu_T|\,|\mathcal{A}|^3)}, \tag{54}$$

where $\sigma_T \neq 0$ is a nondegenerate linear coefficient and g_T is the cubic saturation coefficient.

Theorem 10 (Turing criticality)**.** *Assume* (43) *and suppose* (47) *holds for an admissible Neumann mode $k = k_c > 0$, and that the standard nondegeneracy conditions in Appendix B are satisfied. Then:*

- *If $g_T > 0$, the Turing bifurcation is supercritical: a branch of small-amplitude stable stationary patterns exists for $\mu_T > 0$ (with amplitude $|\mathcal{A}| \sim \sqrt{\mu_T}$).*
- *If $g_T < 0$, the Turing bifurcation is subcritical: patterns emerge for $\mu_T < 0$ and the weakly nonlinear branch is unstable, signaling bistability/hysteresis at higher order.*

The coefficient g_T is given in closed form in Appendix B.

4.7 Turing–Hopf interaction and coupled amplitude equations

A *Turing–Hopf (TH) codimension–two point* occurs when the ODE Hopf condition $\tau = 0$ (equivalently $B = B_H$ from (18)) coincides with the Turing

threshold (47) for some admissible $k_c > 0$:

$$\begin{aligned} &\tau = 0,\ \delta > 0,\ Q > 0,\ Q^2 = 4D_u D_v\,\delta, \\ &k_c^2 = \frac{Q}{2D_u D_v} \in \{k_{mn}^2 : (m,n) \neq (0,0)\}. \end{aligned} \tag{55}$$

Near such a point, the center subspace is three–dimensional: a complex Hopf mode ($k = 0$) and a real stationary Turing mode ($k = k_c$). The standard normal–form reduction [6,15] yields the coupled amplitude system

$$\boxed{\begin{aligned} \dot{\mathcal{H}} &= (\sigma_H \mu_H + i\omega_H)\mathcal{H} + \ell_1(A,\alpha)\,\mathcal{H}|\mathcal{H}|^2 + \chi_H\,\mathcal{H}\,\mathcal{T}^2 + \text{h.o.t.}, \\ \dot{\mathcal{T}} &= \sigma_T \mu_T\,\mathcal{T} - g_T\,\mathcal{T}^3 - \chi_T\,\mathcal{T}|\mathcal{H}|^2 + \text{h.o.t.}, \end{aligned}} \tag{56}$$

where $\mathcal{H}(T) \in \mathbb{C}$ is the Hopf amplitude, $\mathcal{T}(T) \in \mathbb{R}$ is the Turing amplitude, $\omega_H > 0$ is the Hopf frequency, and μ_H, μ_T are unfolding parameters transverse to the Hopf and Turing curves. Here $\ell_1(A,\alpha)$ is precisely the ODE first Lyapunov coefficient already computed (Theorem 7), while g_T, χ_H, χ_T are determined by the kinetics and diffusion through explicit closed–form formulas (Appendix B).

Remark (Interpretation). System (56) captures the local competition between temporal oscillations (Hopf) and stationary spatial patterns (Turing). For $A > \alpha \geq 0$, the corrected closed form in Section 3 gives $\Re\ell_1(A,\alpha) = \ell_1(A,\alpha) < 0$, hence the homogeneous Hopf mode is *supercritical* throughout the admissible Hopf curve. Consequently, the remaining local scenario classification near a TH point is governed by the Turing cubic coefficient g_T and the coupling coefficients (χ_H, χ_T), which determine whether oscillations suppress or promote stationary patterns (and vice versa). This is the standard weakly nonlinear scenario of Turing–Hopf interaction [6, 15].

5 Numerical simulations and discussion

This section provides a reproducible numerical verification of the analytical results obtained in Sections 2, 3 and 4. We first validate diffusion–driven

instability leading to *stationary* Turing patterns in the Neumann reaction–diffusion system (37). We then illustrate the *codimension-two Turing–Hopf interaction*, where a Hopf-unstable homogeneous mode ($k = 0$) coexists with a finite-wavenumber Turing instability, producing spatiotemporal (breathing) structures.

5.1 Parameter set and linear predictions

Throughout we fix

$$A = 1.5, \qquad \alpha = 0.3,$$

so that the Hopf threshold from (18) is $B_H \approx 1.947368$. To isolate a *pure Turing* regime, we choose a parameter value below Hopf,

$$B = 1.85 < B_H, \qquad D_u = 1, \qquad D_v = 20,$$

for which the homogeneous equilibrium (u^*, v^*) exists and is stable for the spatially homogeneous ODE (cf. Section 3). Indeed,

$$(u^*, v^*) = \Big(A,\ \frac{B(1+\alpha A)}{A - \alpha B}\Big) = \big(1.500000,\ 2.838624\big),$$

and the Jacobian of the reaction kinetics at (u^*, v^*) has

$$\tau = -0.127586 < 0, \qquad \delta = 0.615879 > 0, \qquad \tau^2 - 4\delta = -2.447239 < 0,$$

so the ODE equilibrium is a *stable focus*. On the other hand, the diffusion-weighted coefficient

$$Q := D_u g_v + D_v f_u = 9.149983 > 0$$

satisfies $Q^2 > 4 D_u D_v \delta$, hence there is a Turing unstable band of Neumann wavenumbers $k \in (k_-, k_+)$, where (cf. Section 4)

$$k_\pm^2 = \frac{Q \pm \sqrt{Q^2 - 4 D_u D_v \delta}}{2 D_u D_v}, \qquad k_*^2 = \frac{Q}{2 D_u D_v}.$$

For this parameter set,

$$k_-^2 \approx 0.08201,\ k_+^2 \approx 0.375489,\ k_*^2 \approx 0.22875,$$

$$k_- \approx 0.286374,\ k_+ \approx 0.612771,\ k_* \approx 0.478278.$$

Thus, while the spatially homogeneous mode $k = 0$ is stable ($\tau < 0$), a finite band of Neumann modes is linearly unstable; this is the classical diffusion–driven (Turing) mechanism [6, 22, 32].

5.2 Numerical method (Neumann cosine discretization)

We solve (37) on a square $\Omega = (0, L) \times (0, L)$ with $L = 30$ using a cosine pseudo–spectral discretization compatible with Neumann boundary conditions: the Laplacian is diagonal in the cosine basis with eigenvalues $-k_{mn}^2$. Time integration uses an IMEX first–order scheme: diffusion is treated implicitly in spectral space, while the nonlinear reaction terms are treated explicitly in physical space. Concretely, if $\widehat{u}_{mn}^n, \widehat{v}_{mn}^n$ denote cosine coefficients at time t_n and $\widehat{F}_{mn}^n, \widehat{G}_{mn}^n$ those of the reaction terms, then

$$\widehat{u}_{mn}^{n+1} = \frac{\widehat{u}_{mn}^n + \Delta t\, \widehat{F}_{mn}^n}{1 + \Delta t\, D_u k_{mn}^2}, \qquad \widehat{v}_{mn}^{n+1} = \frac{\widehat{v}_{mn}^n + \Delta t\, \widehat{G}_{mn}^n}{1 + \Delta t\, D_v k_{mn}^2}.$$

Initial data are small random perturbations of the homogeneous equilibrium,

$$u(x, y, 0) = u^*\big(1 + \varepsilon \xi_1(x, y)\big), \qquad v(x, y, 0) = v^*\big(1 + \varepsilon \xi_2(x, y)\big),$$

with $\varepsilon = 10^{-2}$ and ξ_1, ξ_2 i.i.d. mean-zero unit-variance noise; we fix a random seed in the code for exact reproducibility. Unless stated otherwise, we use a 192×192 grid, time step $\Delta t = 0.04$, and integrate up to $T = 250$. Time series are sampled at the representative point $(x_0, y_0) = (L/2, L/2)$.

5.3 Diffusion–driven instability and pattern formation

Figure 4 shows the dispersion curve $k^2 \mapsto \max \Re\lambda(k)$ together with the admissible Neumann eigenvalues k_{mn}^2 for $L = 30$. A positive growth rate is

observed on a finite band, and the most unstable admissible mode for this domain is detected as $(m, n) = (0, 4)$; in particular, this mode lies inside the predicted unstable band $k \in (k_-, k_+)$ and is of the same scale as the continuous maximizer $k \approx k_*$.

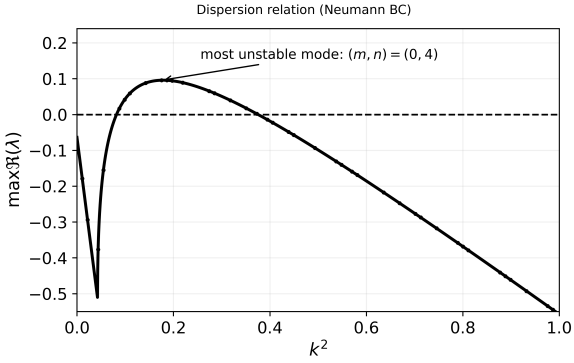

Figure 4. Dispersion curve for the linearization of (37) about (u^*, v^*) under Neumann BC for $A = 1.5$, $\alpha = 0.3$, $B = 1.85$, $D_u = 1$, $D_v = 20$. Black dots mark admissible Neumann eigenvalues k_{mn}^2 for $L_x = L_y = 30$; the most unstable admissible mode is annotated.

The nonlinear evolution saturates the linear growth and converges to a stationary spatial pattern. A representative final-time snapshot of the pattern is shown in Fig. 5. The time series at a fixed point and the L^2-deviation from the homogeneous equilibrium confirm growth followed by saturation to a steady (non-oscillatory) patterned state; see Fig. 6.

The numerical experiments corroborate the analytical classification in Section 4: for $B < B_H$ the homogeneous equilibrium is asymptotically stable for the kinetic ODE, yet sufficiently large diffusion contrast ($D_v \gg D_u$) destabilizes a finite band of Neumann modes, leading to robust stationary patterns. This provides a clean verification of Turing instability in the crowding-modified Brusselator kinetics (37) under Neumann boundary conditions.

To emphasize that pattern selection is constrained by the discrete Neumann spectrum, we also plot the growth rate evaluated only on admissible modes. Figure 7 shows that only a finite set of (m, n) satisfies

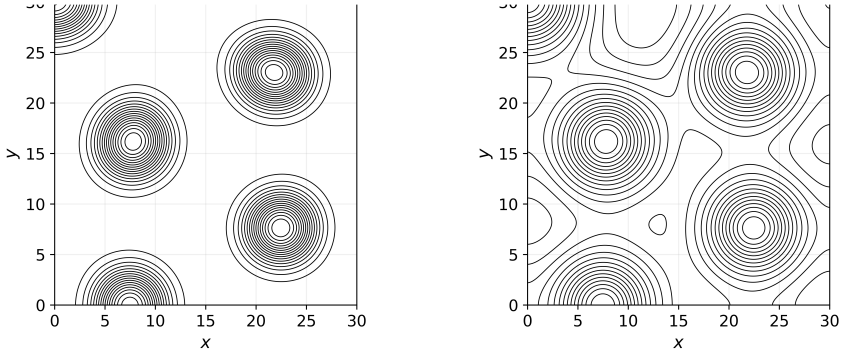

Figure 5. Stationary Turing pattern obtained from (37) under Neumann BC on $(0, 30) \times (0, 30)$ for $A = 1.5$, $\alpha = 0.3$, $B = 1.85$, $D_u = 1$, $D_v = 20$. Shown are black/white line-contour snapshots of $u(x, y, T)$ and $v(x, y, T)$ at $T = 250$.

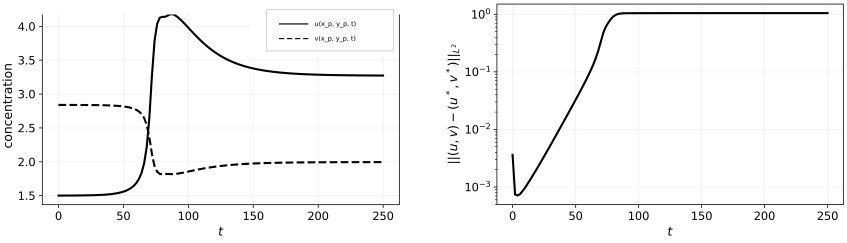

(a) Time series at $(x_0, y_0) = (L/2, L/2)$.

(b) L^2 deviation $||(u, v) - (u^*, v^*)||_{L^2}$ (log scale).

Figure 6. Growth and saturation of the diffusion-driven instability for the same parameters as Fig. 5. The dynamics converges to a *stationary* patterned state (Turing pattern), in agreement with ODE stability ($\tau < 0$) and the finite-k instability band.

$\max \Re\lambda_{mn} > 0$, and the dominant admissible instability is $(m, n) = (0, 4)$, consistent with the continuous dispersion peak in Fig. 4.

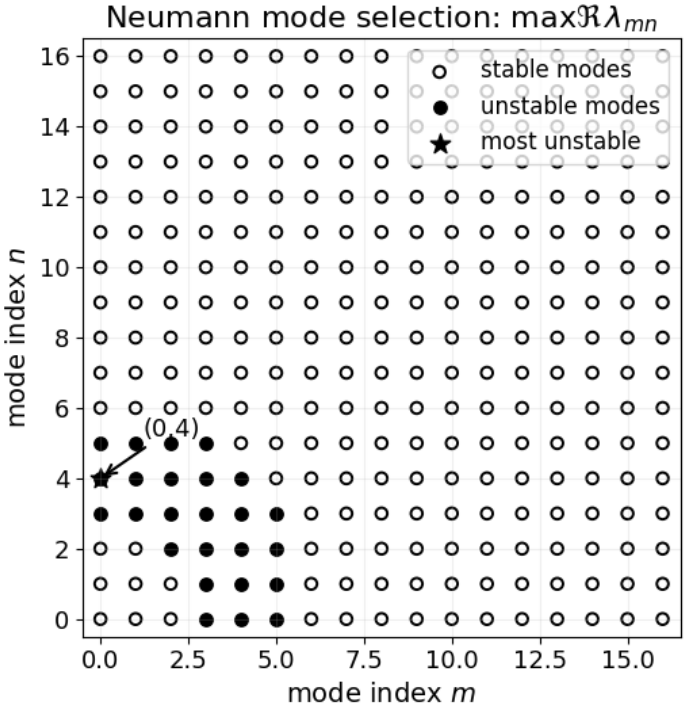

Figure 7. Discrete Neumann mode selection for the same parameter set as Fig. 4. Each lattice point (m, n) corresponds to the Neumann eigenmode ϕ_{mn} with wavenumber $k_{mn}^2 = (m\pi/L)^2 + (n\pi/L)^2$. Filled markers indicate $\max \Re\lambda_{mn} > 0$ (unstable modes), open markers indicate stability, and the star marks the most unstable admissible mode, here $(m, n) = (0, 4)$.

Next, Fig. 8 summarizes how the diffusion-driven mechanism varies with the control parameter B at fixed diffusion contrast. The curve plots $\max_{k \geq 0} \max \Re\lambda(k)$; thus, positivity directly indicates a Turing-unstable regime. Marking B_H clarifies that our selected value $B = 1.85$ lies below Hopf (stable kinetics at $k = 0$) while still supporting finite-k growth, yielding a clean stationary-pattern regime.

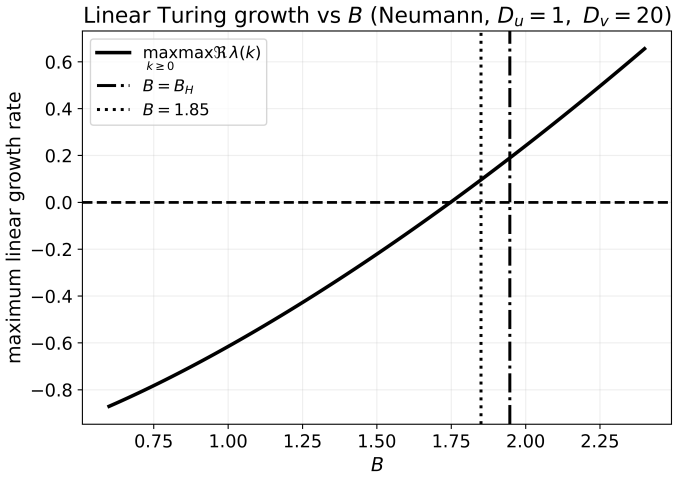

Figure 8. Maximum linear growth rate $\max_{k \geq 0} \max \Re\lambda(k)$ as a function of B for $A = 1.5$, $\alpha = 0.3$, $D_u = 1$, $D_v = 20$ (Neumann setting). The Hopf threshold $B = B_H$ is indicated, and the choice $B = 1.85$ used in Figs. 4–6 is marked. Positive values correspond to diffusion-driven instability.

5.4 Codimension-two Turing–Hopf interaction and breathing patterns

We next demonstrate numerically the spatiotemporal regime created near the *Turing–Hopf* codimension-two point, where the homogeneous Hopf threshold and the diffusion-driven (Turing) threshold intersect in a two-parameter plane. In the present model (37), Hopf instability of the spatially homogeneous kinetics is controlled by $B = B_H$ (Section 3), while diffusion-driven instability is controlled by the diffusion contrast (Section 4). At a Turing–Hopf point, the linearization has a pair of purely imaginary eigenvalues at $k = 0$ (Hopf) and simultaneously a real eigenvalue crossing at some $k = k_c > 0$ (Turing). Consequently, one expects *spatiotemporal* patterns with oscillatory modulation of the dominant spatial mode ("breathing").

Parameter selection near the Turing–Hopf point. We keep $A = 1.5$, $\alpha = 0.3$, and $D_u = 1$ fixed, and vary (B, D_v). Figure 9 shows the Hopf line $B = B_H$ together with the Turing threshold curve $D_v^+(B)$ (for the first

unstable Neumann band), and indicates the numerically chosen simulation point near their intersection.

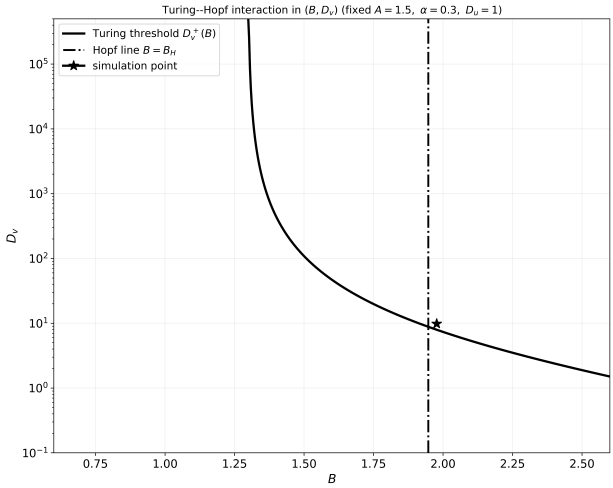

Figure 9. Turing–Hopf interaction in the (B, D_v) plane for fixed $A = 1.5$, $\alpha = 0.3$, $D_u = 1$. The dash–dot vertical line is the Hopf threshold $B = B_H$ for the spatially homogeneous kinetics (Section 3), and the solid curve is the Turing threshold $D_v^+(B)$ from the diffusion-driven instability conditions (Section 4). The marked point indicates the simulation parameter choice used in Figs. 10–11.

Temporal oscillation and mode-amplitude modulation. To verify the presence of a Hopf component together with a dominant spatial mode, we record (i) a probe-point time series and (ii) the amplitude of the dominant Neumann cosine mode (m, n) detected from the evolving solution via the cosine spectral coefficients of $(u - u^*, v - v^*)$. Figure 10 shows a clear temporal modulation, and it confirms growth and subsequent saturation/modulation of the dominant spatial mode amplitude.

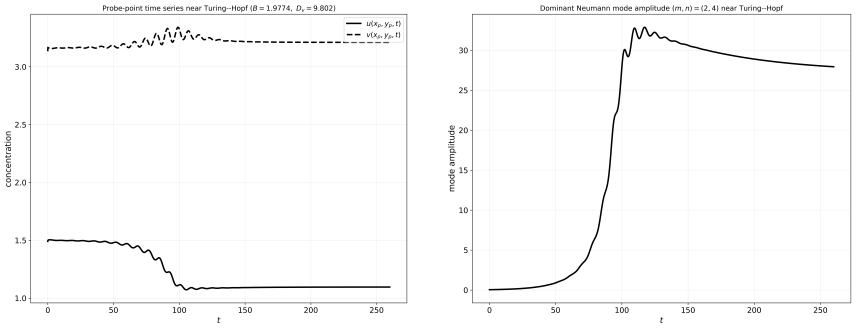

(a) Probe-point time series $u(x_p, y_p, t)$ and $v(x_p, y_p, t)$.

(b) Amplitude of the dominant Neumann mode (from cosine coefficients).

Figure 10. Time oscillations and dominant-mode modulation near a Turing–Hopf point for the Neumann problem (37).

Breathing spatial structure. Finally, Fig. 11 plots black/white line-contour snapshots of $u(x, y, t)$ at three times $t = t_1 < t_2 < t_3$. The spatial structure persists while its amplitude varies in time, which is characteristic of a Turing–Hopf interaction (spatiotemporal "breathing" patterns).

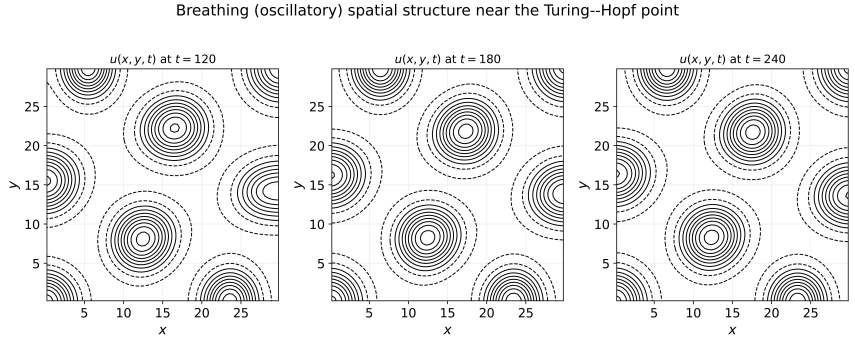

Figure 11. Breathing spatial structure near the Turing–Hopf interaction point: line-contour snapshots of $u(x, y, t)$ at three times, showing persistent spatial organization with oscillatory temporal modulation.

The simulations complement the stationary-pattern results above. For $B < B_H$, the homogeneous kinetics is stable and diffusion may destabilize only a finite band of modes, producing stationary Turing patterns (Section 5.3 and Fig. 5). Near the codimension-two Turing–Hopf interaction,

the $k = 0$ Hopf mechanism and the finite-k Turing mechanism coexist, producing spatiotemporal patterns with oscillatory mode modulation, as confirmed by Figs. 9–11.

6 Conclusion

In this work we proposed and analyzed a crowding–limited Brusselator that incorporates volume–exclusion effects in a deliberately minimal and analytically tractable manner. The classical autocatalytic feedback is modified by a rational free–volume factor depending on the total local occupancy, while the linear feed and decay structure is retained. As a result, the model introduces a single crowding parameter α that interpolates continuously between the dilute mass–action regime and increasingly constrained intracellular/microfluidic environments, thereby providing a clean mathematical platform for quantifying how excluded volume reshapes the canonical Brusselator dynamics.

From a dynamical systems viewpoint, the analysis yields a complete and explicit description of the well–mixed (ODE) kinetics on the biologically/chemically relevant positive quadrant. We established positivity and forward invariance, constructed parameter–dependent a priori bounds leading to dissipativity, and proved permanence under explicit hypotheses, which places the long–time dynamics on a compact invariant set. The unique positive equilibrium E_* was obtained in closed form and shown to be feasible precisely under $A > \alpha B$, revealing how crowding reduces the admissible parameter range for sustained autocatalysis. A full linear stability classification was then derived in terms of trace–determinant criteria, allowing the equilibrium to be organized into stable and unstable regimes without relying on numerical continuation.

A central outcome is the fully explicit Hopf bifurcation structure. We derived the Hopf threshold curve in closed form and verified transversality, establishing that the loss of stability of E_* proceeds through a generic Hopf mechanism. Importantly, the first Lyapunov coefficient was computed explicitly, yielding a parameter–dependent criterion that determines whether the emerging oscillations are supercritical (stable small cycles) or subcritical

(unstable small cycles and potential hysteresis). This closed–form criticality result is particularly useful for chemical kinetics because it provides a direct diagnostic for oscillation onset and robustness in terms of experimentally interpretable parameters: the feed level, the effective decay rate, and the crowding strength. In this sense, the crowding–limited model not only generalizes the classical Brusselator but also retains the key advantage that has made the Brusselator a benchmark: explicit bifurcation boundaries that can be mapped and compared across regimes.

We further extended the kinetics to a two–dimensional reaction–diffusion system with Neumann boundary conditions, which is the natural idealization for closed or no–flux microreactors and intracellular subdomains. The Neumann cosine spectrum yields explicit modal growth rates and a transparent dispersion relation, from which we derived analytic conditions for diffusion–driven (Turing) instability. In addition, we characterized the codimension–two Turing–Hopf interaction where stationary pattern selection and temporal oscillation interact, and we carried out a weakly nonlinear reduction to obtain amplitude equations governing the near–threshold evolution. These results provide a coherent link between crowding–modified reaction propensities and the classical pattern–formation mechanism: crowding changes the effective nonlinear feedback and thus shifts not only the Hopf threshold but also the location and character of patterning windows in parameter space.

The numerical experiments support and complement the theoretical analysis. In the ODE setting, simulations confirm the Hopf predictions, including the emergence of periodic orbits and the expected small–amplitude scaling near onset. In the spatial model, numerics corroborate the linear stability boundaries and illustrate how stationary Turing patterns and spatiotemporal structures arise as parameters cross the analytically derived thresholds. Together, the analysis and computations demonstrate that even a single crowding parameter can reorganize the classical Brusselator landscape, shifting and reshaping oscillatory and patterned regimes in a way that is relevant to crowded chemical and biochemical environments.

Despite these strengths, the present study has limitations that point naturally to future work. First, the crowding mechanism is deliberately coarse:

it compresses complex excluded–volume and anomalous transport effects into a single rational suppression term. More detailed constitutive choices (e.g., activity coefficients, nonlinear diffusion, or crowding–dependent cross–diffusion) may be required to match specific experimental systems. Second, the spatial analysis is carried out for constant diffusivities and Neumann boundaries on a simple two–dimensional domain; intracellular geometries are often heterogeneous and compartmentalized, and diffusion can be effectively spatially varying or anisotropic. Third, while weakly nonlinear amplitude equations clarify local pattern selection near thresholds, global pattern competition, defect dynamics, and far–from–onset transitions are not addressed here. Finally, the model is deterministic; in microfluidic and intracellular settings, intrinsic noise (finite copy number) and extrinsic fluctuations can be comparable to deterministic drift near bifurcation thresholds and may fundamentally affect onset, coherence, and pattern selection.

Several extensions therefore merit investigation. A first direction is to incorporate stochasticity via chemical Langevin equations or stochastic reaction–diffusion formulations, and to quantify how noise interacts with Hopf, Turing, and Turing–Hopf thresholds (e.g., coherence resonance, noise–induced patterning, or switching near subcritical regimes). A second direction is to move beyond constant diffusion and consider crowding–dependent transport, nonlinear diffusion, or cross–diffusion terms that arise naturally from free–volume and excluded–volume considerations, and to study their influence on dispersion relations and amplitude reductions. A third direction is geometric and multiscale: extending the analysis to three dimensions, irregular domains, and heterogeneous boundary conditions relevant to synthetic cells and compartmentalized microreactors. Finally, experimental validation would be valuable, for instance by implementing controlled crowding in microfluidic reactors or synthetic vesicles and measuring how oscillation onset and spatial patterning windows shift with effective occupancy. Such studies would help calibrate the minimal free–volume law used here and identify when more detailed crowding physics is required.

Overall, the crowding–limited Brusselator developed here provides a

mathematically explicit bridge between intracellular crowding concepts and classical nonlinear chemical dynamics. By retaining a minimal structure while enabling closed–form bifurcation and patterning theory, the model offers a useful reference point for future analytical, computational, and experimental investigations of oscillations and self–organization beyond the dilute limit.

A Multilinear-form evaluation of ℓ_1 in Section 3

Following [14, 19], write the Taylor expansion at $\mu = 0$ in the form

$$\dot{\xi} = J_H \xi + \frac{1}{2}\,\mathcal{B}(\xi,\xi) + \frac{1}{6}\,\mathcal{C}(\xi,\xi,\xi) + \mathcal{O}(\|\xi\|^4), \qquad \xi = (u,v)^\top,$$

where $\mathcal{B}$ and $\mathcal{C}$ are defined by the (symmetric) second and third derivatives. In terms of the coefficients in (28),

$$\mathcal{B}(\eta,\zeta) = \begin{pmatrix} a_{20}\eta_1\zeta_1 + a_{11}(\eta_1\zeta_2 + \eta_2\zeta_1) + a_{02}\eta_2\zeta_2 \\ b_{20}\eta_1\zeta_1 + b_{11}(\eta_1\zeta_2 + \eta_2\zeta_1) + b_{02}\eta_2\zeta_2 \end{pmatrix},$$

and, for brevity, define

$$S_{112} := \sum_{\text{sym}} \eta_1\zeta_1\theta_2, \qquad S_{122} := \sum_{\text{sym}} \eta_1\zeta_2\theta_2.$$

Then

$$\mathcal{C}(\eta,\zeta,\theta) = \begin{pmatrix} a_{30}\eta_1\zeta_1\theta_1 + a_{21}S_{112} + a_{12}S_{122} + a_{03}\eta_2\zeta_2\theta_2 \\ b_{30}\eta_1\zeta_1\theta_1 + b_{21}S_{112} + b_{12}S_{122} + b_{03}\eta_2\zeta_2\theta_2 \end{pmatrix},$$

where

$$S_{112} = \eta_1\zeta_1\theta_2 + \eta_1\zeta_2\theta_1 + \eta_2\zeta_1\theta_1, \qquad S_{122} = \eta_1\zeta_2\theta_2 + \eta_2\zeta_1\theta_2 + \eta_2\zeta_2\theta_1.$$

Let q be the right eigenvector of J_H for $i\omega_H$ and let p be the left eigenvector of J_H for $-i\omega_H$, normalized by $\langle p, q\rangle = 1$ (standard complex

inner product). With the explicit choice

$$q = \begin{pmatrix} 1 \\ -1 + i/\omega_H \end{pmatrix}, \qquad p = \begin{pmatrix} \frac{1+i\omega_H}{2} \\ \frac{i\omega_H}{2} \end{pmatrix}, \qquad \langle p, q \rangle = 1,$$

define the auxiliary vectors

$$h_{20} = (2i\omega_H I - J_H)^{-1}\mathcal{B}(q, q), \qquad h_{11} = J_H^{-1}\mathcal{B}(q, \bar{q}).$$

Then the standard Kuznetsov–Hassard expression gives

$$c_1 = \frac{1}{2}\langle p, \mathcal{C}(q, q, \bar{q})\rangle - \langle p, \mathcal{B}(q, h_{11})\rangle + \frac{1}{2}\langle p, \mathcal{B}(\bar{q}, h_{20})\rangle, \qquad \ell_1 = \frac{1}{2\omega_H}\Re(c_1),$$

which is exactly the convention used in Section 3.

Substituting the closed-form coefficients (30)–(31), evaluating c_1, and simplifying yields the explicit closed form

$$\ell_1(A, \alpha) = \ell_1(A, \alpha) = -\frac{6A^2\alpha^2 + 6A\alpha + A^2 + 2}{4A^2(1 + \alpha A)^{3/2}(A - \alpha)},$$

which matches (35). This completes the derivation of the Hopf normal form (33) and Theorem 7.

B Closed–form derivative tensors and amplitude coefficients for Section 4

Throughout, $E_* = (u^*, v^*)$ is the positive homogeneous equilibrium (39) and J_* is the Jacobian at E_* (that is, $J(E_*)$). We write the Taylor expansion of the reaction field at E_* as

$$F(\xi) = J_*\xi + \frac{1}{2}\,\mathcal{B}(\xi, \xi) + \frac{1}{6}\,\mathcal{C}(\xi, \xi, \xi) + \mathcal{O}(\|\xi\|^4), \qquad \xi = (\xi_1, \xi_2)^\top, \quad (57)$$

where $\mathcal{B}$ and $\mathcal{C}$ are the symmetric bilinear and trilinear forms defined componentwise by second and third derivatives at E_*.

B.1 All second and third derivatives at E_* in closed form

Let f, g be defined by (38). Denote partial derivatives at E_* by $f^*_{uu} = \partial_u^2 f(E_*)$, $f^*_{uv} = \partial_u \partial_v f(E_*)$, etc. Then the *complete* list of second derivatives is

$$\boxed{\begin{aligned} f^*_{uu} &= \frac{2B(1+\alpha^2 B)^2}{A(1+\alpha A)^2}, \\ f^*_{uv} &= \frac{(A-\alpha B)^2\,(2+\alpha A+2\alpha^2 B)}{A(1+\alpha A)^2}, \\ f^*_{vv} &= -\frac{2\alpha(A-\alpha B)^3}{A(1+\alpha A)^2}, \\ g^*_{uu} &= -f^*_{uu},\ g^*_{uv} = -f^*_{uv}, \\ g^*_{vv} &= -f^*_{vv}. \end{aligned}} \tag{58}$$

The *complete* list of third derivatives is

$$\boxed{\begin{aligned} f^*_{uuu} &= -\frac{6B\alpha(A-\alpha B)(1+\alpha^2 B)^2}{A^2(1+\alpha A)^3}, \\ f^*_{uuv} &= \frac{2(A-\alpha B)^2(1+\alpha^2 B)(1+3\alpha^2 B)}{A^2(1+\alpha A)^3}, \\ f^*_{uvv} &= -\frac{2\alpha(A-\alpha B)^3(2+3\alpha^2 B)}{A^2(1+\alpha A)^3}, \\ f^*_{vvv} &= \frac{6\alpha^2(A-\alpha B)^4}{A^2(1+\alpha A)^3}, \end{aligned}} \qquad \boxed{\begin{aligned} g^*_{uuu} &= -f^*_{uuu}, \\ g^*_{uuv} &= -f^*_{uuv}, \\ g^*_{uvv} &= -f^*_{uvv}, \\ g^*_{vvv} &= -f^*_{vvv}. \end{aligned}} \tag{59}$$

With these, the multilinear forms in (57) are explicitly

$$\mathcal{B}(\eta,\zeta) = \begin{pmatrix} f^*_{uu}\eta_1\zeta_1 + f^*_{uv}(\eta_1\zeta_2+\eta_2\zeta_1) + f^*_{vv}\eta_2\zeta_2 \\ g^*_{uu}\eta_1\zeta_1 + g^*_{uv}(\eta_1\zeta_2+\eta_2\zeta_1) + g^*_{vv}\eta_2\zeta_2 \end{pmatrix}, \tag{60}$$

and, for $\eta \in \mathbb{R}^2$,

$$\mathcal{C}(\eta,\eta,\eta) = \begin{pmatrix} f^*_{uuu}\eta_1^3 + 3f^*_{uuv}\eta_1^2\eta_2 + 3f^*_{uvv}\eta_1\eta_2^2 + f^*_{vvv}\eta_2^3 \\ g^*_{uuu}\eta_1^3 + 3g^*_{uuv}\eta_1^2\eta_2 + 3g^*_{uvv}\eta_1\eta_2^2 + g^*_{vvv}\eta_2^3 \end{pmatrix}. \tag{61}$$

B.2 Closed form for Q and the Turing threshold

Recall $Q = D_u g_v^* + D_v f_u^*$ from (44). Using the closed forms of f_u^*, g_v^* from $J(E_*)$, one obtains

$$\boxed{Q = \frac{D_v\big(B - 1 - \alpha A + \alpha^2 B^2\big) - D_u(A - \alpha B)^2}{1 + \alpha A}.} \tag{62}$$

Likewise, the ODE determinant $\delta = \det(J_*)$ is already in closed form in the ODE part; the Turing threshold condition (47) is therefore an explicit algebraic constraint in (A, B, α, D_u, D_v).

B.3 Turing cubic coefficient g_T

Let $k_c > 0$ satisfy (47)–(48). Define the linear operators (on modal amplitudes)

$$\mathcal{L}_k := J_* - k^2 D, \qquad D = \mathrm{diag}(D_u, D_v).$$

At the critical Turing mode, $\mathcal{L}_{k_c}$ has a simple zero eigenvalue. Write $\mathcal{L}_{k_c} = \begin{pmatrix} \tilde{a}_{11} & a_{12} \\ a_{21} & \tilde{a}_{22} \end{pmatrix}$ with $\tilde{a}_{11} = f_u^* - D_u k_c^2$, $\tilde{a}_{22} = g_v^* - D_v k_c^2$, $a_{12} = f_v^*$, $a_{21} = g_u^*$.

A convenient (unscaled) right kernel vector is

$$p := \begin{pmatrix} a_{12} \\ -\tilde{a}_{11} \end{pmatrix}, \qquad \mathcal{L}_{k_c} p = 0, \tag{63}$$

and a corresponding left kernel vector for $\mathcal{L}_{k_c}$ is obtained from the transpose:

$$\tilde{q} := \begin{pmatrix} a_{21} \\ -\tilde{a}_{11} \end{pmatrix}, \qquad \mathcal{L}_{k_c}^{\top} \tilde{q} = 0. \tag{64}$$

Normalize by $q := \tilde{q}/\langle \tilde{q}, p \rangle$, so that $\langle q, p \rangle = 1$.

The quadratic interaction of the critical mode produces a mean ($k = 0$) component and a second harmonic ($k = 2k_c$). Accordingly define w_{20} and w_{11} by the *exact* linear systems

$$\boxed{\mathcal{L}_0 w_{20} = -\mathcal{B}(p, p), \qquad \mathcal{L}_{2k_c} w_{11} = -\mathcal{B}(p, p),} \tag{65}$$

where $\mathcal{B}$ is given explicitly by (60). Since $\mathcal{L}_0 = J_*$ is invertible under $\delta > 0$, and $\mathcal{L}_{2k_c}$ is invertible at the simple Turing threshold, these have the closed-form solutions

$$\boxed{w_{20} = -\mathcal{L}_0^{-1}\mathcal{B}(p,p), \qquad w_{11} = -\mathcal{L}_{2k_c}^{-1}\mathcal{B}(p,p),} \tag{66}$$

where, for any 2×2 matrix $M = \begin{pmatrix} m_{11} & m_{12} \\ m_{21} & m_{22} \end{pmatrix}$ with $\det(M) \neq 0$,

$$M^{-1} = \frac{1}{\det(M)} \begin{pmatrix} m_{22} & -m_{12} \\ -m_{21} & m_{11} \end{pmatrix}.$$

Finally, the cubic Landau coefficient in (54) is

$$\boxed{g_T = \frac{1}{6}\left\langle q, \mathcal{C}(p,p,p)\right\rangle + \frac{1}{2}\Big\langle q, \mathcal{B}\big(p, w_{11}\big) + \frac{1}{2}\,\mathcal{B}\big(p, w_{20}\big)\Big\rangle,} \tag{67}$$

where $\mathcal{C}(p,p,p)$ is given explicitly by (61). Equations (58)–(59) provide *all* derivative coefficients needed to evaluate (67) in closed form.

C Closed-form computations for the Turing–Hopf point and amplitude coefficients

This appendix collects the lengthy algebra used in Subsection 4.5 and Remark 4.5. All notation is consistent with Sections 2–4.

C.1 Equilibrium identities and Jacobian simplifications

Let

$$\begin{aligned} h(u,v) &:= \frac{u^2 v}{1+\alpha(u+v)}, \\ F(u,v) &= A - (B+1)u + h(u,v), \\ G(u,v) &= Bu - h(u,v). \end{aligned}$$

The homogeneous equilibrium in $\mathbb{R}^2_{>0}$ is

$$u^* = A, \qquad v^* = \frac{B(1+\alpha A)}{A-\alpha B}, \text{ assuming } A > \alpha B.$$

Define the convenient abbreviations

$$S := A - \alpha B, \qquad T := 1 + \alpha A, \text{ so that } S > 0,\ T > 1.$$

At (u^*, v^*) one has the identity (from $G(u^*, v^*) = 0$)

$$\frac{v^*}{1+\alpha(u^*+v^*)} = \frac{B}{A},\ 1+\alpha(u^*+v^*) = \frac{AT}{S}. \tag{68}$$

First derivatives of h. Let $D(u, v) := 1 + \alpha(u + v)$. Then

$$h(u, v) = \frac{u^2 v}{D}.$$

A direct differentiation yields

$$h_u = \frac{2uv}{D} - \frac{\alpha u^2 v}{D^2},\ h_v = \frac{u^2}{D} - \frac{\alpha u^2 v}{D^2}. \tag{69}$$

Evaluating at (u^*, v^*) and using (68) gives

$$\boxed{h^*_u = 2B - \frac{\alpha BS}{T},\ h^*_v = \frac{S^2}{T}.} \tag{70}$$

Hence the kinetic Jacobian $J = \begin{pmatrix} f_u & f_v \\ g_u & g_v \end{pmatrix}$ at (u^*, v^*) satisfies

$$\boxed{f_u = -(B+1) + h^*_u = B - 1 - \frac{\alpha BS}{T}, f_v = h^*_v = \frac{S^2}{T},} \tag{71}$$

$$\boxed{g_u = B - h^*_u = -B + \frac{\alpha BS}{T}, g_v = -h^*_v = -\frac{S^2}{T}.} \tag{72}$$

Therefore,

$$\boxed{\begin{aligned}&\delta = \det(J) = \frac{S^2}{T},\\ &\tau = \mathrm{tr}(J) = f_u + g_v = B - 1 - \frac{AS}{T},\\ &\Delta = \tau^2 - 4\delta.\end{aligned}} \tag{73}$$

In particular, at the Hopf threshold $\tau = 0$ one recovers (18), and

$$\boxed{\delta_H = \delta\big|_{B=B_H} = \frac{(A-\alpha)^2(1+\alpha A)}{(1+2\alpha A)^2},} \tag{74}$$

as stated in (50). Moreover, substituting $\tau = 0$ into (73) gives

$$B_H - 1 = \frac{AS_H}{T}, \text{ where } S_H := A - \alpha B_H = \frac{(A-\alpha)T}{1+2\alpha A}.$$

Using these identities in (71)–(72) yields the Hopf simplification

$$\boxed{\text{at } B = B_H: \ f_u = \delta_H, \quad f_v = \delta_H, \quad g_v = -\delta_H.} \tag{75}$$

C.2 Turing threshold curve and codimension–two point

Recall $Q := D_u g_v + D_v f_u$. Using (71)–(72) gives the closed form

$$\boxed{Q(B, D_v) = -D_u \frac{S^2}{T} + D_v \left(B - 1 - \frac{\alpha B S}{T}\right).} \tag{76}$$

The continuous-spectrum Turing threshold is characterized by

$$Q > 0, \qquad Q^2 = 4D_u D_v\, \delta, \qquad k_c^2 = \frac{Q}{2D_u D_v},$$

where $\delta = S^2/T$. Substituting (76) and $\delta = S^2/T$ into $Q^2 = 4D_u D_v\, \delta$ yields a quadratic equation for D_v:

$$\big(f_u(B)\big)^2 D_v^2 - 2D_u\delta(B)\big(f_u(B) + 2\big)D_v + D_u^2\delta(B)^2 = 0, \tag{77}$$

where $f_u(B)$ and $\delta(B)$ are given by (71) and (73). Solving (77) gives the two-branch Turing threshold:

$$\boxed{\begin{aligned} D_v^{\pm}(B) =& D_u\,\delta(B)\,\frac{f_u(B)+2\pm 2\sqrt{f_u(B)+1}}{\big(f_u(B)\big)^2} \\ =& D_u\,\delta(B)\,\frac{\big(\sqrt{f_u(B)+1}\pm 1\big)^2}{\big(f_u(B)\big)^2}, \end{aligned}} \tag{78}$$

valid whenever $f_u(B) > -1$ and $A > \alpha B$. At the codimension–two point, $\tau = 0$ (i.e. $B = B_H$), and (75) implies $f_u = \delta_H$ and

$$Q = \delta_H(D_v - D_u).$$

Then $Q^2 = 4D_uD_v\,\delta_H$ yields (51) and

$$k_c^2 = \frac{Q}{2D_uD_v} = \frac{\delta_H(D_v - D_u)}{2D_uD_v},$$

i.e. (52).

C.3 Amplitude-equation coefficients in multilinear-form closed form

We outline the full coefficient computation for the Turing–Hopf normal form (53) by a standard center-manifold / multiple-scales reduction (cf. [6,15,22]). Let $U = (u, v)^\top$ and write (37) as

$$U_t = \mathcal{L}U + \mathcal{N}(U), \qquad \mathcal{L} = \begin{pmatrix} D_u\Delta & 0 \\ 0 & D_v\Delta \end{pmatrix} + J,$$

where J is evaluated at (u^*, v^*) and $\mathcal{N}(U)$ collects quadratic and higher terms in $U - (u^*, v^*)$.

Let $q \in \mathbb{C}^2$ be the eigenvector of J associated with $+i\omega_H$ at Hopf ($k = 0$), and let $p \in \mathbb{C}^2$ be the adjoint eigenvector of $J^\top$ associated with $-i\omega_H$, normalized by $\langle p, q\rangle = 1$ (standard Euclidean inner product on $\mathbb{C}^2$). Let $w \in \mathbb{R}^2$ be the (real) eigenvector associated with the zero eigenvalue at

the Turing mode $k = k_c$ at the threshold. Define the symmetric multilinear forms of the reaction vector field at (u^*, v^*):

$$B(\xi, \eta) = \frac{1}{2} D^2 \mathcal{R}(U^*)[\xi, \eta], \qquad C(\xi, \eta, \zeta) = \frac{1}{6} D^3 \mathcal{R}(U^*)[\xi, \eta, \zeta],$$

where $\mathcal{R} = (F, G)^\top$ denotes the reaction part. All entries of $D^2\mathcal{R}(U^*)$ and $D^3\mathcal{R}(U^*)$ are explicit rational expressions in (A, B, α) obtained by differentiating (69); these derivatives are lengthy but elementary, and can be recorded term-by-term if the editor requests (they are omitted here only for readability).

With the standard solvability projection, one obtains the cubic coefficients

$$\begin{aligned} a_1 = \langle p,\, C(q, q, \bar{q})\rangle - 2\langle p,\, B(q, \mathcal{L}_0^{-1} B(q, \bar{q}))\rangle \\ + \langle p,\, B(\bar{q}, (2i\omega_H I - \mathcal{L}_0)^{-1} B(q, q))\rangle. \end{aligned}$$

and similarly the cross-coupling

$$\begin{aligned} a_2 = \langle p,\, C(q, w, w)\rangle - 2\langle p,\, B(q, \mathcal{L}_{k_c}^{-1} B(w, w))\rangle \\ - \langle p,\, B(w, (\mathcal{L}_{k_c} - i\omega_H I)^{-1} B(q, w))\rangle. \end{aligned}$$

where $\mathcal{L}_0$ and $\mathcal{L}_{k_c}$ denote the linear operators restricted to the $k = 0$ and $k = k_c$ eigenspaces (including diffusion contributions). Analogous formulas yield b_1 and b_2 by projecting onto the adjoint Turing eigenvector. These expressions are *closed form* once the derivatives of $\mathcal{R}$ are substituted and the resolvents are evaluated (all are 2×2 matrix inverses in this setting). We refer to (53) for the final normal-form structure used in the main text.

C.4 Turing–Hopf coupling coefficients χ_H, χ_T

At a TH point (55), the reduced system (56) involves the ODE Hopf Lyapunov coefficient $\ell_1(A, \alpha)$ (already computed in the ODE section, in corrected closed form) and the coefficients g_T above together with χ_H, χ_T. The latter are obtained by the same projection/solvability procedure as in the classical TH normal form [6, 15]: one expands the center manifold including mixed interactions between the Hopf mode ($k = 0$) and the Turing mode ($k = k_c$), solves the resulting forced linear systems using the resolvents $\mathcal{L}_0^{-1}$, $\mathcal{L}_{k_c}^{-1}$ on the stable complement, and projects the cubic terms onto the critical directions using the normalized left eigenvectors.

All forcing terms are expressed solely via the multilinear forms $\mathcal{B}, \mathcal{C}$, hence ultimately via the explicit derivative lists (58)–(59).

References

[1] K. Bar–Eli, On the stability of coupled chemical oscillators, *Physica D* **14** (1985) 242–252.

[2] D. Bullara, Y. De Decker, R. Lefever, Confined Turing patterns in the Brusselator model with volume exclusion, *Phys. Rev. E* **87** (2013) #062923.

[3] G. J. Butler, H. I. Freedman, P. Waltman, Uniformly persistent systems, *Proc. Am. Math. Soc.* **96** (1986) 425–430.

[4] R. G. Casten, C. J. Holland, Instability results for reaction–diffusion equations with Neumann boundary conditions, *J. Diff. Eq.* **27** (1978) 266–273.

[5] V. Castets, E. Dulos, J. Boissonade, P. De Kepper, Experimental evidence of a sustained standing Turing–type nonequilibrium chemical pattern, *Phys. Rev. Lett.* **64** (1990) 2953–2956.

[6] M. C. Cross, P. C. Hohenberg, Pattern formation outside of equilibrium, *Rev. Mod. Phys.* **65** (1993) 851–1112.

[7] J. A. Dix, A. S. Verkman, Crowding effects on diffusion in solutions and cells, *Ann. Rev. Biophys.* **37** (2008) 247–263.

[8] L. Edelstein–Keshet, *Mathematical Models in Biology*, SIAM, Philadelphia, 2005.

[9] I. R. Epstein, J. A. Pojman, *An Introduction to Nonlinear Chemical Dynamics: Oscillations, Waves, Patterns, and Chaos*, Oxford Univ. Press, New York, 1998.

[10] A. Gierer, H. Meinhardt, A theory of biological pattern formation, *Kybernetik* **12** (1972) 30–39.

[11] P. Gray, S. K. Scott, Autocatalytic reactions in the isothermal, continuous stirred tank reactor: Oscillations and instabilities in the system $A + 2B \to 3B$, $B \to C$, *Chem. Eng. Sci.* **39** (1984) 1087–1097.

[12] P. Grindrod, *Patterns and Waves: The Theory and Applications of Reaction–Diffusion Equations*, Oxford Univ. Press, Oxford, 1991.

[13] J. Guckenheimer, P. Holmes, *Nonlinear Oscillations, Dynamical Systems, and Bifurcations of Vector Fields*, Springer, New York, 2002.

[14] B. D. Hassard, N. D. Kazarinoff, Y. H. Wan, *Theory and Applications of Hopf Bifurcation*, Cambridge Univ. Press, Cambridge, 1981.

[15] R. Hoyle, *Pattern Formation: An Introduction to Methods*, Cambridge Univ. Press, Cambridge, 2006.

[16] V. Hutson, K. Schmitt, Permanence and the dynamics of biological systems, *Math. Biosci.* **111** (1992) 1–71.

[17] R. Kapral, K. Showalter (Eds.), *Chemical Waves and Patterns*, Kluwer Acad. Pub., Dordrecht, 1995.

[18] S. Kondo, T. Miura, Reaction–diffusion model as a framework for understanding biological pattern formation, *Science* **329** (2010) 1616–1620.

[19] Y. A. Kuznetsov, *Elements of Applied Bifurcation Theory*, Springer, New York, 2004.

[20] R. Lefever, G. Nicolis, Chemical instabilities and sustained oscillations, *J. Theor. Biol.* **30** (1971) 267–284.

[21] A. P. Minton, The influence of macromolecular crowding and confinement on biochemical reactions in physiological media, *J. Biol. Chem.* **276** (2001) 10577–10580.

[22] J. D. Murray, *Mathematical Biology II: Spatial Models and Biomedical Applications*, Springer, New York, 2003.

[23] Q. Ouyang, H. L. Swinney, Transition from a uniform state to hexagonal and striped Turing patterns, *Nature* **352** (1991) 610–612.

[24] J. E. Pearson, Complex patterns in a simple system, *Science* **261** (1993) 189–192.

[25] I. Prigogine, R. Lefever, Symmetry breaking instabilities in dissipative systems. II, *J. Chem. Phys.* **48** (1968) 1695–1700.

[26] G. Rivas, A. P. Minton, Macromolecular crowding in vitro, in vivo, and in between, *Trends Biochem. Sci.* **41** (2016) 970–981.

[27] J. Schnakenberg, Simple chemical reaction systems with limit cycle behaviour, *J. Theor. Biol.* **81** (1979) 389–400.

[28] S. Schnell, T. E. Turner, Reaction kinetics in intracellular environments with macromolecular crowding: simulations and rate laws, *Prog. Biophys. Mol. Biol.* **85** (2004) 235–260.

[29] H. L. Smith, H. R. Thieme, *Dynamical Systems and Population Persistence*, Am. Math. Soc., Providence, 2011.

[30] S. H. Strogatz, *Nonlinear Dynamics and Chaos*, Westview Press, Boulder, 2015.

[31] R. Q. Sun, J. F. Li, H. D. Zhang, Y. L. Yang, Kinetic pattern formation with intermolecular interactions: A modified brusselator model, *Chin. J. Polym. Sci.* **39** (2021) 1673–1679.

[32] A. M. Turing, The chemical basis of morphogenesis, *Phil. Trans. Royal Soc. London B* **237** (1952) 37–72.

[33] A. T. Winfree, *The Geometry of Biological Time*, Springer, New York, 2001.

[34] H. X. Zhou, G. Rivas, A. P. Minton, Macromolecular crowding and confinement: biochemical, biophysical, and potential physiological consequences, *Ann. Rev. Biophys.* **37** (2008) 375–397.